NASA TECHNICAL NOTE

NASA TN D-6203

THE COMPRESSIBLE TURBULENT BOUNDARY LAYER ON A BLUNT SWEPT SLAB WITH AND WITHOUT LEADING-EDGE BLOWING

by James L. Hunt, Dennis M. Bushnell,
and Ivan E. Beckwith

Langley Research Center
Hampton, Va. 23365

NATIONAL AERONAUTICS AND SPACE ADMINISTRATION • WASHINGTON, D. C. • MARCH 1971

1. Report No. NASA TN D-6203	2. Government Accession No.	3. Recipient's Catalog No.
4. Title and Subtitle THE COMPRESSIBLE TURBULENT BOUNDARY LAYER ON A BLUNT SWEPT SLAB WITH AND WITHOUT LEADING-EDGE BLOWING		5. Report Date March 1971
		6. Performing Organization Code
7. Author(s) James L. Hunt, Dennis M. Bushnell, and Ivan E. Beckwith		8. Performing Organization Report No. L-7433
9. Performing Organization Name and Address NASA Langley Research Center Hampton, Va. 23365		10. Work Unit No. 129-01-20-07
		11. Contract or Grant No.
12. Sponsoring Agency Name and Address National Aeronautics and Space Administration Washington, D.C. 20546		13. Type of Report and Period Covered Technical Note
		14. Sponsoring Agency Code

15. Supplementary Notes

This paper is an extension of paper no. 19 in NASA SP-228, 1970.

16. Abstract

A finite-difference method has been developed to solve the equations for compressible turbulent boundary layers on swept infinite cylinders. Predictions of surface heating are compared with experimental data on a 60° swept, blunt, slab configuration with and without leading-edge blowing. The test conditions were a free-stream Mach number of 8, a wall-to-total temperature ratio of 0.4, and a range of free-stream Reynolds number, based on leading-edge diameter, from 0.92×10^5 to 9.3×10^5. Predictions for surface streamlines, Mach number profiles, and boundary-layer thickness have also been compared with experimental data, but for zero blowing only.

These comparisons indicated that for test Reynolds numbers of 2.6×10^5 or larger, the leading-edge boundary layer was turbulent. As the flow expanded around the leading edge onto the slab, the turbulent boundary was apparently laminarized. The chordwise location of the apparent laminarization was influenced by the leading-edge blowing at the largest test blowing rates. Tentative conclusions regarding the validity of assumed eddy-viscosity models for three-dimensional turbulent boundary layers have also been obtained.

17. Key Words (Suggested by Author(s)) Compressible Turbulent Boundary layer Blunt swept slab Leading-edge blowing	18. Distribution Statement Unclassified – Unlimited		
19. Security Classif. (of this report) Unclassified	20. Security Classif. (of this page) Unclassified	21. No. of Pages 61	22. Price* $3.00

THE COMPRESSIBLE TURBULENT BOUNDARY LAYER ON A BLUNT

SWEPT SLAB WITH AND WITHOUT LEADING-EDGE BLOWING[*]

By James L. Hunt, Dennis M. Bushnell,
and Ivan E. Beckwith
Langley Research Center

SUMMARY

A finite-difference method has been developed to solve the equations for compressible turbulent boundary layers on swept infinite cylinders. Predictions by this method have been compared with experimental data on a 60° swept, blunt, slab configuration with and without leading-edge blowing. The test conditions were a free-stream Mach number of 8, a wall-to-total temperature ratio of 0.4, and a range of free-stream Reynolds number based on leading-edge diameter $N_{Re,\infty}$ from 0.92×10^5 to 9.3×10^5.

Three different approaches to the formulation of eddy-viscosity models for three-dimensional boundary layers were considered. Two of these formulations were used in the numerical solutions. Nonsimilar solutions for laminar flow were obtained by setting the eddy viscosity equal to zero.

Predictions for heat transfer, surface streamlines, Mach number profiles, and boundary-layer thickness have been compared with experimental data for zero blowing. These comparisons indicated that for $N_{Re,\infty} = 2.6 \times 10^5$, the leading-edge boundary layer was turbulent, but as the flow expanded around the leading edge, the measured properties of the boundary layer on the slab portion of the model approached those predicted for a laminar boundary layer. This apparent laminarization of the initially turbulent boundary layer was probably caused by the large streamwise pressure gradients and the rapid expansion of the flow in the leading-edge region. At the higher test Reynolds number of 9.3×10^5, transition back to turbulent flow was observed on the downstream part of the slab. Both eddy-viscosity models gave satisfactory predictions of the turbulent flow, provided the mixing length in the outer part of the boundary layer was taken as 0.05 of the boundary-layer thickness. This fraction is generally larger on flat-plate turbulent boundary layers where values up to 0.10 have been used. The smaller values of the ratio required to obtain agreement between theory and the present data suggest that the level of turbulence in the present three-dimensional boundary layers was small compared with flat-plate flows at high Reynolds numbers.

[*]This paper is an extension of paper no. 19 in NASA SP-228, 1970.

The hypothesis of low turbulence levels in the leading-edge boundary layers of these tests was also consistent with the apparent laminarization phenomenon since the value of a parameter that characterizes the onset of laminarization was an order of magnitude below the critical levels observed for laminarization in two-dimensional flow. The small value of this parameter suggests that the turbulent boundary layer on the leading edge was highly susceptible to laminarization as would be expected if the initial turbulence levels were small.

The measured heating rates with blowing indicated that the laminarization-like behavior and the subsequent transition back to turbulent flow were essentially independent of leading-edge blowing for the smallest blowing rates used in this investigation. However, when the blowing rate was increased by about 40 percent, the measured heating rates remained at the higher turbulent levels for about 2 leading-edge diameters farther downstream.

INTRODUCTION

The boundary layers on large lifting vehicles are predominantly turbulent and three dimensional in nature. For such vehicles, the accurate prediction of frictional drag is essential. As the flight Mach numbers are increased above approximately 3, reliable predictions of heat transfer also become important, especially on windward and leading-edge regions where active or passive cooling systems are required.

The boundary-layer flows on the windward and leading-edge regions of these large lifting vehicles can often be classified as belonging to a particular type of three-dimensional flow designated as quasi-two-dimensional since the governing equations can be expressed in terms of only two independent variables. If transition from laminar flow has occurred far upstream of the region of interest, the turbulent boundary layers on sharp cones at small angles of attack and on infinite cylinders at yaw belong to this class of flows. These flows may exhibit significant three-dimensional effects since the velocity vector within the boundary layer may have large components normal to the external inviscid streamline direction. The boundary-layer velocity component in this direction is generally referred to as the cross flow.

Several previous methods developed for the calculation of compressible boundary layers of this quasi-two-dimensional class, as well as more general three-dimensional flows, were integral methods (refs. 1 to 5). The assumption of small (or zero) cross flow within the boundary layer was used in references 3 to 5. As shown by the results of reference 5, the assumption of small cross flow is generally more valid for turbulent flows than for laminar ones. This assumption requires that the magnitude of the velocity normal to the inviscid streamlines and the derivatives in that direction be

2

small; thus, it follows that the component of the surface shear normal to the inviscid streamline is small and has a negligible effect on the streamwise flow which develops independently of the cross flow. (See ref. 6, for example.) The Reynolds stress in the streamwise direction is then independent of the cross flow, and two-dimensional models for the Reynolds stress are directly applicable.

For large streamline curvature and large surface blowing, the cross flow in turbulent boundary layers may be large. With large cross flows, the shear stress normal to the inviscid streamlines influences the streamwise flow, and the two-dimensional models of the Reynolds stress may no longer be adequate. Thus, boundary-layer solutions in the presence of large cross flows necessitate the formulation of models for both components of Reynolds stress (streamwise and cross flow) that will properly account for the three-dimensional nature of the flow. A finite-difference procedure for solving the equations for incompressible turbulent boundary layers without the small-cross-flow assumption has been developed by Nash (ref. 7) who assumed that the magnitude of the shear stress is proportional to the turbulent intensity.

A finite-difference method is utilized herein which is applicable to compressible boundary-layer flows in the presence of large cross flows and surface blowing. This method of solution consists of the extension of the finite-difference procedure of reference 8 to include the spanwise momentum equation for swept infinite cylinders. The computational advantages of two independent variables are thereby retained, while the boundary layer may have large cross-flow components. The computations are not carried out in streamline coordinates, and the only restrictions are those arising from the assumed models for the components of the Reynolds stress in the chordwise and spanwise directions and for the turbulent flux of enthalpy.

The purpose of this investigation is to evaluate the proposed Reynolds stress models by comparison of theoretical predictions with new experimental data obtained on a 60° swept slab with and without homogeneous blowing at the leading edge. The test conditions were a free-stream Mach number of 8, a wall-to-total temperature ratio of 0.4, and free-stream Reynolds numbers, based on leading-edge diameter, from 0.92×10^5 to 9.3×10^5. Several solutions for test Reynolds numbers of 2.6×10^5 and 9.3×10^5 have been obtained with various combinations of two eddy-viscosity models and different mixing-length functions. The results are compared with measurements of wall heat transfer, oil-flow lines (representing surface streamlines), Mach number profiles, and boundary-layer thickness. The region of special interest is just downstream of the blunt leading edge where the boundary-layer profiles are far from equilibrium because of the upstream conditions of blowing and large cross-flow pressure gradients.

This paper extends the results and analysis of reference 9 to include additional data at higher blowing rates for a Reynolds number of 2.6×10^5.

A   area

A^* function of blowing parameter (see ref. 8)

$a_i, b_i, c_i, d_i, e_i, f_i$ temperature coefficients in heat-balance matrix (34)

B   normalized blowing rate, $\dfrac{(\rho v)_w}{(\rho u)_e}$

C_f skin-friction coefficient, $\dfrac{\tau_w}{\frac{1}{2}\rho_e u_e{}^2}$

c   specific heat of model material

c_p specific heat at constant pressure

d   leading-edge diameter

G   eddy-viscosity function defined by equation (19)

g_i constants in heat-balance matrix (34)

H   total enthalpy, $h + \dfrac{u^2 + w^2}{2}$

h   static enthalpy

h^* heat-transfer coefficient

k   molecular thermal conductivity

L   reference length

l mixing length (eqs. (8) and (9))

M   Mach number (based on local velocity vector q)

$\dot{m}$ mass flow rate per unit area

$N_{Pr,T}$ turbulent Prandtl number based on static enthalpy, $\dfrac{c_p \epsilon}{\kappa}$

$N_{Re,s}$ reference Reynolds number, $\dfrac{\rho_s \sqrt{2H_e}\, L}{\mu_s}$

$N_{Re,\infty}$ free-stream Reynolds number based on leading-edge diameter, $\dfrac{\rho_\infty q_\infty d}{\mu_\infty}$

N_{St} Stanton number, $\dfrac{h^*}{\rho_e u_e (h_{aw} - h)}$

$\bar{n}$ exponent in transformation (eqs. (26))

p pressure

$\dot{q}$ heat-transfer rate per unit area per unit time

q local velocity vector, $\sqrt{u^2 + w^2}$

R ideal gas constant

s distance along an inviscid streamline

T absolute temperature

t time

u,v,w velocity components in x-, y-, and z-directions (fig. 1)

$\tilde{v} = \bar{v} + \dfrac{\overline{\rho' v'}}{\bar{\rho}}$

V volume

x,y,z Cartesian coordinate system (fig. 1), also coordinate system used in heat-conduction problem (fig. 21)

α permeability, ft^2, $\dfrac{2\dot{m}\, \Delta Y (\mu RT)_w}{p_c^2 - p_w^2}$

ΔY wall thickness of porous leading edge

Δy wall thickness at thermocouple stations on slab

δ	boundary-layer thickness, usually evaluated at the point where $\dfrac{M}{M_e} \approx 0.995$
ϵ	eddy viscosity
ϵ^*	emissivity
θ	angle between z-coordinate direction and local velocity vector
κ	eddy thermal conductivity (eq. (7))
Λ	leading-edge sweep
μ	molecular viscosity
ξ,η	transformed coordinate system (eqs. (26))
ρ	mass density
σ	Boltzmann constant
τ	shear stress

Subscripts:

aw	adiabatic wall
c	coolant conditions inside porous leading edge before injection
e	local "edge" of boundary layer
g	gas
m	model material
max	maximum
min	minimum
n	direction parallel to surface and normal to local inviscid streamline

o   initial condition at time zero

p   direction parallel to the surface and parallel to the local inviscid streamline

r   local reference condition, may be either wall or edge

s   stagnation line

T   turbulent

t   total

w   wall or outside surface of model

x,y,z   in the x-, y-, or z-direction

∞   free-stream flow in tunnel

A bar over a symbol indicates a mean quantity. A prime indicates a fluctuating quantity.

ANALYTICAL METHOD

Numerical solutions to the partial differential equations for the boundary layer on swept infinite cylinders are obtained by an implicit finite-difference procedure. The method of reference 8 for two-dimensional and axisymmetric flows is extended to swept cylinders by including the spanwise momentum equation. The Reynolds stress terms in the momentum equations are formulated by the use of eddy-viscosity concepts. The turbulent flux of static enthalpy is related to the Reynolds stress by the turbulent Prandtl number.

The formulation of models for the eddy viscosity in three-dimensional boundary layers is of primary concern herein. Two different models for the eddy viscosity are utilized in the calculations: (1) the "invariant turbulence" model, in which the total shear is treated as a vector and the eddy viscosity is assumed independent of direction and (2) Lettau's vorticity-transfer hypothesis (ref. 10), in which the change of vorticity following a turbulent eddy is expressed in a general vector form.

Boundary-Layer Equations

The coordinate system for the idealized flow model is shown in figure 1(a). The instantaneous flow variables in the general conservation equations are divided into mean and fluctuating parts, and the Reynolds averaging process is applied. The following equations are then obtained after the higher order terms are neglected according to the usual order-of-magnitude analysis for thin boundary layers:

Continuity

$$\frac{\partial}{\partial x}(\bar{\rho}\bar{u}) + \frac{\partial}{\partial y}(\bar{\rho}\tilde{v}) = 0 \tag{1}$$

Chordwise momentum

$$\bar{\rho}\bar{u}\,\frac{\partial \bar{u}}{\partial x} + \bar{\rho}\tilde{v}\,\frac{\partial \bar{u}}{\partial y} = -\frac{\partial \bar{p}}{\partial x} + \frac{\partial}{\partial y}\left(\bar{\mu}\,\frac{\partial \bar{u}}{\partial y} - \bar{\rho}\,\overline{v'u'}\right) \tag{2}$$

Spanwise momentum

$$\bar{\rho}\bar{u}\,\frac{\partial \overline{w}}{\partial x} + \bar{\rho}\tilde{v}\,\frac{\partial \overline{w}}{\partial y} = \frac{\partial}{\partial y}\left(\bar{\mu}\,\frac{\partial \overline{w}}{\partial y} - \bar{\rho}\,\overline{v'w'}\right) \tag{3}$$

Energy

$$\bar{\rho}\bar{u}\,\frac{\partial \overline{H}}{\partial x} + \bar{\rho}\tilde{v}\,\frac{\partial \overline{H}}{\partial y} = \frac{\partial}{\partial y}\left[\frac{\bar{k}}{c_p}\,\frac{\partial \bar{h}}{\partial y} - \bar{\rho}\,\overline{v'h'} - \bar{\rho}\bar{u}\,\overline{v'u'} - \bar{\rho}\overline{w}\,\overline{v'w'} + \bar{\mu}\,\frac{\partial}{\partial y}\left(\frac{\overline{u}^2 + \overline{w}^2}{2}\right)\right] \tag{4}$$

These equations are valid in the entire stagnation region of a cylinder if a characteristic Reynolds number, based on the radius of curvature of the leading edge, is large. (See ref. 11.)

Before equations (1) to (4) can be solved, expressions must be supplied for the Reynolds stress or turbulent shear terms in the momentum equations and the turbulent flux of enthalpy in the total-enthalpy equations. The approach used in the present method is to model these terms as functions of the mean-flow variables.

Eddy Diffusivity Coefficients

The concept that the Reynolds stress in turbulent flow is proportional to a momentum exchange coefficient times the mean-flow velocity gradient was first proposed by Boussinesq, as discussed in reference 12. This concept is based on an assumed analogy between eddy viscosity and molecular viscosity. The shear components in the chordwise and spanwise directions are then written as

SWEPT INFINITE CYLINDER
$$w_e = w_\infty; \frac{\partial}{\partial z} (\overline{}) = 0$$
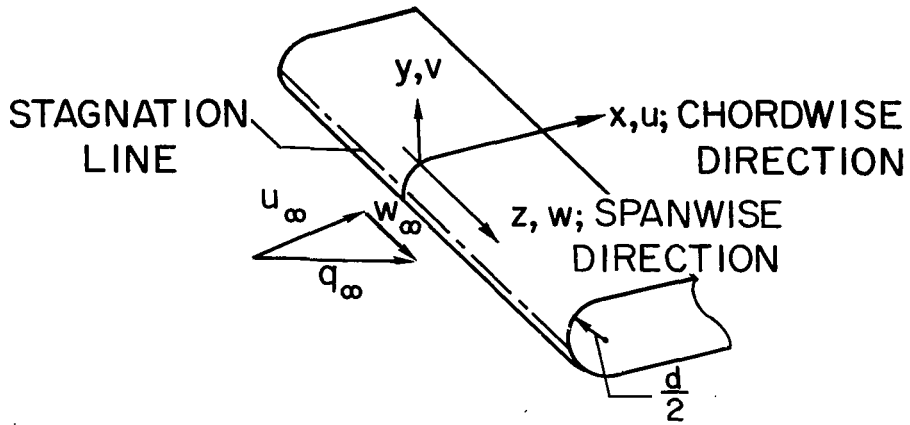
(a) Idealized flow model.
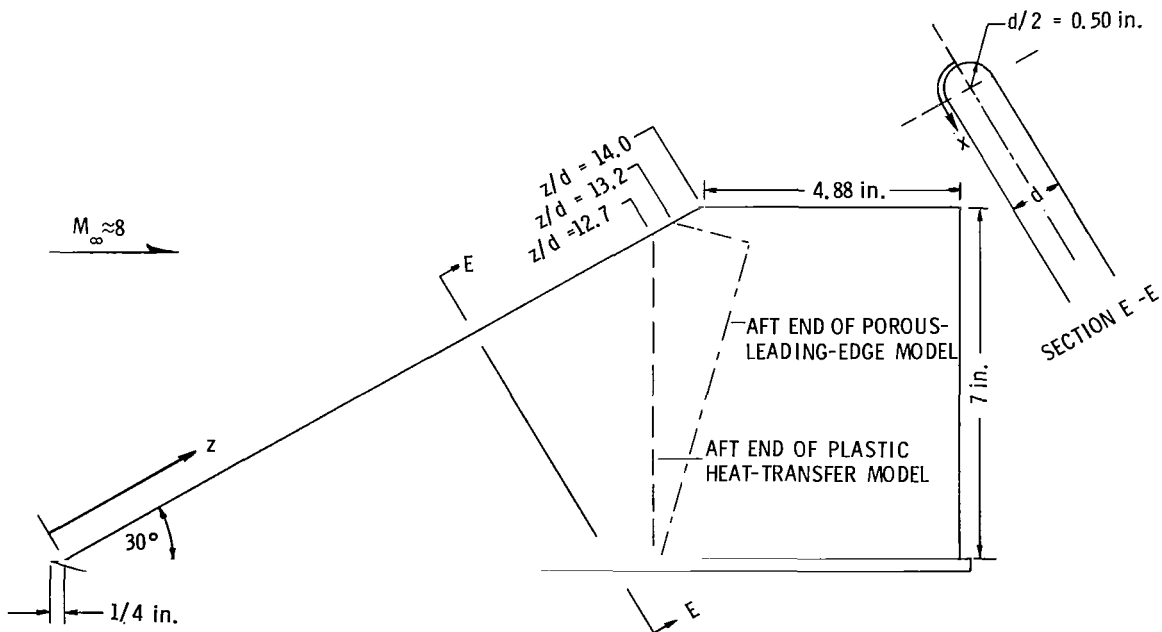
(b) Test model configurations.

Figure 1.- Basic model configuration and coordinate definitions.

$$\left. \begin{array}{l} \tau_x = \bar{\mu} \dfrac{\partial \bar{u}}{\partial y} - \bar{\rho} \overline{v'u'} \approx \bar{\mu} \dfrac{\partial \bar{u}}{\partial y} + \epsilon_x \dfrac{\partial \bar{u}}{\partial y} \\[3mm] \tau_z = \bar{\mu} \dfrac{\partial \overline{w}}{\partial y} - \bar{\rho} \overline{v'w'} \approx \bar{\mu} \dfrac{\partial \overline{w}}{\partial y} + \epsilon_z \dfrac{\partial \overline{w}}{\partial y} \end{array} \right\} \tag{5}$$

where the eddy viscosities in the x- and z-directions might in general be different. Since the total shear can be treated approximately as a vector quantity in boundary-layer flows, its magnitude may be written as

$$\tau = \left(\tau_x{}^2 + \tau_y{}^2 \right)^{1/2} = \left[\left(\bar{\mu} + \epsilon_x \right)^2 \left(\dfrac{\partial \bar{u}}{\partial y} \right)^2 + \left(\bar{\mu} + \epsilon_z \right)^2 \left(\dfrac{\partial \overline{w}}{\partial y} \right)^2 \right]^{1/2} \tag{6}$$

The eddy thermal conductivity κ is defined in a manner similar to that used in equations (5) for the eddy viscosity. The total heat flux in equation (4) is then expressed as

$$\dot{q} = \dfrac{\bar{k}}{c_p} \dfrac{\partial \bar{h}}{\partial y} - \bar{\rho} \overline{v'h'} \approx \dfrac{\bar{k}}{c_p} \dfrac{\partial \bar{h}}{\partial y} + \dfrac{\kappa}{c_p} \dfrac{\partial \bar{h}}{\partial y} \tag{7}$$

The remaining two fluctuating terms in equation (4) are products of velocity and Reynolds stress; thus, they are modeled according to equations (5).

Eddy-Viscosity Models

The simplest approach to the formulation of models for the Reynolds stress is based on Prandtl's mixing-length hypothesis (ref. 13). For two-dimensional flow, this hypothesis states that

$$\left. \begin{array}{l} u' \propto -l \dfrac{\partial \bar{u}}{\partial y} \\[3mm] v' \propto l \left| \dfrac{\partial \bar{u}}{\partial y} \right| \end{array} \right\} \tag{8}$$

The turbulent shear and eddy viscosity are then

$$\tau_T \equiv -\bar{\rho} \overline{v'u'} = \bar{\rho} l^2 \left| \dfrac{\partial \bar{u}}{\partial y} \right| \dfrac{\partial \bar{u}}{\partial y} \tag{9}$$

$$\epsilon = \bar{\rho} l^2 \left| \dfrac{\partial \bar{u}}{\partial y} \right| \tag{10}$$

where the quantity l is the mixing length, which is presumably related to some characteristic length of the turbulent motion. In the near-wall region of a boundary layer, l is

10

assumed to be proportional to the distance from the wall. In the far-wall region or in free turbulence, l is assumed to be proportional to the width of the mixing layer, that is, to the boundary-layer thickness or the width of the mixing jet. Although the details of such a transfer mechanism are not well understood, the basic concept gives satisfactory results even at hypersonic Mach numbers in the presence of large heat transfer and large pressure gradients. (See refs. 8 and 14.) One purpose of the present paper is to determine whether the basic mixing-length concept can be extended to three-dimensional flows. Three different approaches to this problem are considered.

Independence principle.- The chordwise development of the laminar, incompressible boundary layer on a swept infinite cylinder is independent of the spanwise flow. (See ref. 15.) This concept is referred to as the "independence principle." The application of this principle to turbulent flow was first attempted by Young and Booth. (See ref. 16.) Although the variable density in compressible flow couples the chordwise and spanwise momentum equations, it is of interest to consider whether a valid mixing-length expression for the Reynolds stress can be formulated from the independence principle. Thus, if the chordwise flow is independent of the spanwise flow, the chordwise shear would have to be of the form

$$\tau_{x,T} = \bar{\rho} l_x{}^2 \left| \frac{\partial \bar{u}}{\partial y} \right| \frac{\partial \bar{u}}{\partial y} \tag{11}$$

The simplest expression for the spanwise shear that retains the correct form at the stagnation line is

$$z_{x,T} = \bar{\rho} l_z{}^2 \left| \frac{\partial \overline{w}}{\partial y} \right| \frac{\partial \overline{w}}{\partial y} \tag{12}$$

The resulting expressions for the eddy viscosities are

$$\left.\begin{aligned} \epsilon_x &= \bar{\rho} l_x{}^2 \left| \frac{\partial \bar{u}}{\partial y} \right| \\[2mm] \epsilon_z &= \bar{\rho} l_z{}^2 \left| \frac{\partial \overline{w}}{\partial y} \right| \end{aligned}\right\} \tag{13}$$

Hence the eddy viscosities are different in the two directions and therefore depend on coordinate direction. The turbulent Prandtl number would then presumably be based on the "total" eddy viscosity, with the result that

$$N_{Pr,T} = \frac{c_p}{\kappa} \sqrt{\epsilon_x{}^2 + \epsilon_z{}^2} \tag{14}$$

However, substitution of equations (13) into equation (6) gives

$$\tau = \left[\left(\bar{\mu} + \bar{\rho} l_x{}^2 \left| \frac{\partial \bar{u}}{\partial y} \right| \right)^2 \left(\frac{\partial \bar{u}}{\partial y} \right)^2 + \left(\bar{\mu} + \bar{\rho} l_z{}^2 \left| \frac{\partial \bar{w}}{\partial y} \right| \right)^2 \left(\frac{\partial \bar{w}}{\partial y} \right)^2 \right]^{1/2} \tag{15}$$

and it is evident that a total eddy viscosity like that of equation (14) cannot be obtained in explicit form from equation (15). The requirement of the independence principle that the eddy viscosity should depend on coordinate direction may therefore be erroneous. Experimental data of Ashkenas and Riddell (ref. 17) also indicate that the independence principle may not apply to turbulent flows. (See also discussion in ref. 18.) In view of these difficulties, the formulation of eddy viscosities from the independence principle will not be pursued further herein.

Invariant turbulence.- An alternate approach to the independence principle is based on the concept that the eddy viscosity should depend only on the properties of the turbulence and a local eddy scale as in the methods of Prandtl (ref. 19) and Glushko (ref. 20). The application of this concept to a mixing-length approach suggests that the eddy viscosity would be a scalar function independent of the coordinate direction. Accordingly, the components of the turbulent shear terms are

$$\left. \begin{aligned} \tau_{x,T} &= \bar{\rho} l^2 \frac{\partial G}{\partial y} \frac{\partial \bar{u}}{\partial y} \\[2em] \tau_{z,T} &= \bar{\rho} l^2 \frac{\partial G}{\partial y} \frac{\partial \bar{w}}{\partial y} \end{aligned} \right\} \tag{16}$$

and the eddy viscosity is then

$$\epsilon = \epsilon_x = \epsilon_z = \bar{\rho} l^2 \frac{\partial G}{\partial y} \tag{17}$$

To determine the scalar function G, equation (17) is substituted into equation (6) to obtain

$$\tau = \left(\bar{\mu} + \bar{\rho} l^2 \frac{\partial G}{\partial y} \right) \left[\left(\frac{\partial \bar{u}}{\partial y} \right)^2 + \left(\frac{\partial \bar{w}}{\partial y} \right)^2 \right]^{1/2} \tag{18}$$

Then by analogy with equations (9) and (10), where the velocity-gradient function for the shear component is repeated in the eddy viscosity, the expression for G is

$$\frac{\partial G}{\partial y} = \left[\left(\frac{\partial \bar{u}}{\partial y} \right)^2 + \left(\frac{\partial \bar{w}}{\partial y} \right)^2 \right]^{1/2} \tag{19}$$

The final expression for the eddy viscosity then becomes

$$\epsilon = \bar{\rho} l^2 \left[\left(\frac{\partial \bar{u}}{\partial y} \right)^2 + \left(\frac{\partial \bar{w}}{\partial y} \right)^2 \right]^{1/2} \tag{20}$$

12

Bradshaw (ref. 21) has derived a set of differential equations for the two components of shear stress based on the Navier-Stokes equations and several assumptions regarding the behavior and formulation of correlation terms for fluctuating pressure and velocity. These equations indicate that the directions of the shear stress components are not generally the same as the directions of the corresponding mean velocity components. However, in the near-wall region, Bradshaw's equations reduce to the same form as the present results (eqs. (18) and (19)).

Lettau's vorticity-transfer hypothesis.- In reference 10, Lettau proposed a modification of Taylor's vorticity-transfer theory, which accounts for the combined action of conservation and adjustment of the vorticity of a fluid element as it is convected along an eddy trajectory. The resulting expressions for the three components of fluctuating velocity reduce to simple forms for the present application. That is, by the use of conventional order-of-magnitude analysis for a thin boundary layer on a swept infinite cylinder, these expressions for the fluctuating velocity components reduce to

$$
\left.
\begin{aligned}
u' &= -l_y \frac{\partial \bar{u}}{\partial y} \\[1em]
v' &= l_x \frac{\partial \bar{u}}{\partial y} + l_z \frac{\partial \overline{w}}{\partial y} \\[1em]
w' &= -l_y \frac{\partial \overline{w}}{\partial y}
\end{aligned}
\right\}
\tag{21}
$$

For simplicity, the various components of an "eddy displacement vector," represented in equations (21) by l_x, l_y, and l_z, are assumed to be independent of direction. The components of the turbulent shear then become

$$
\left.
\begin{aligned}
\tau_{x,T} &\equiv -\bar{\rho}\,\overline{v'u'} = \bar{\rho}l^2\left(\frac{\partial \bar{u}}{\partial y} + \frac{\partial \overline{w}}{\partial y}\right)\frac{\partial \bar{u}}{\partial y} \\[1em]
\tau_{z,T} &\equiv -\bar{\rho}\,\overline{v'w'} = \bar{\rho}l^2\left(\frac{\partial \bar{u}}{\partial y} + \frac{\partial \overline{w}}{\partial y}\right)\frac{\partial \overline{w}}{\partial y}
\end{aligned}
\right\}
\tag{22}
$$

The eddy viscosity is then given by

$$
\epsilon = \bar{\rho}l^2\left(\frac{\partial \bar{u}}{\partial y} + \frac{\partial \overline{w}}{\partial y}\right)
\tag{23}
$$

which is the same for both shear components, but in contrast with the invariant-turbulence model of equation (20), this model is the scalar sum of two vector quantities. Recently, Lettau (ref. 22) has generalized his original hypothesis of reference 10 in an attempt to account for possible variations of his eddy displacement vector and has applied the results to a free-turbulence problem.

Mixing-Length Function

The mixing-length function used for the present calculations is

$$\frac{l}{\delta} = \left[1 - \exp\left(-\frac{\rho_w y}{A^* \mu_w}\sqrt{\frac{\tau_w}{\rho_w}}\right)\right] f\left(\frac{y}{\delta}\right) \tag{24}$$

This expression is the same as the function used in reference 8 except that the gas proper-ties in the exponential are herein always evaluated at the surface, and the function $f(y/\delta)$ is modified to account for smaller levels of turbulence. That is, the f_1 function of ref-erence 8 (table I in ref. 8) was modified by reducing the maximum value of the function for $y/\delta > 0.1$ from 0.09, to 0.07 or 0.05. The Prandtl slope in the near-wall region $\frac{df}{d(y/\delta)} = 0.4$ was retained. Also, the functional dependence of A^* on the blowing param-eter $2B/C_f$ as given in figure 1 of reference 8 has been used in the present calculations.

Variation in Turbulent Prandtl Number

The variation in turbulent Prandtl number through axisymmetric compressible boundary layers with large heat transfer and large favorable pressure gradients is treated extensively in reference 8. The results indicated that values of $N_{Pr,T} = \frac{c_p \epsilon}{\kappa}$ (the "static" turbulent Prandtl number) in the outer part of these boundary layers may be as small as 0.5. Values of $N_{Pr,T}$ obtained from experimental data on flat plates and reported in references 23 and 24 are generally greater than 1.0 near the wall and tend to decrease below 1.0, or in some cases to nearly 0.5, farther from the wall. On the basis of these results, the $N_{Pr,T}$ variation used in all solutions reported herein was taken as a simple ramp function of y/δ as given by the following relations:

$$\left.\begin{aligned} N_{Pr,T} &= 2.0 - 5\frac{y}{\delta} & \left(\frac{y}{\delta} \leq 0.3\right) \\[2ex] N_{Pr,T} &= 0.5 & \left(\frac{y}{\delta} \geq 0.3\right) \end{aligned}\right\} \tag{25}$$

Some check calculations with the alternate assumption of $N_{Pr,T} = 0.9$ reduced the pre-dicted heat transfer by at most 15 percent, which was considered to be within the range of experimental uncertainties. For the present conditions, the choice of the $N_{Pr,T}$ function is apparently not critical.

Numerical Procedure

The Reynolds stress terms in equations (2) and (3) are replaced by the eddy-viscosity expressions (eq. (20) or (23)) with the mixing-length function given by equa-tion (24). These eddy-viscosity and mixing-length expressions are also used in the

energy equation (4) after replacement of the turbulent heat flux by the eddy-conductivity relation of equation (7) and the introduction of $N_{Pr,T}$. The resulting equations are transformed to the coordinate system ξ,η defined by

$$
\left.
\begin{aligned}
\xi\left(\frac{x}{L}\right) &= N_{Re,s} \int_0^{x/L} \frac{(\rho\mu)_r}{(\rho\mu)_s} \frac{u_e}{\sqrt{2H_e}}\, d\left(\frac{x}{L}\right) \\[2ex]
\eta\left(\frac{x}{L},\frac{y}{L}\right) &= N_{Re,s} \frac{u_e/\sqrt{2H_e}}{(2\xi)^{\bar{n}}} \int_0^{y/L} \frac{\bar{\rho}}{\rho_s}\, d\left(\frac{y}{L}\right)
\end{aligned}
\right\}
\tag{26}
$$

where $\bar{n}$ is adjusted to obtain a nearly constant boundary-layer thickness in the ξ,η plane in order to increase the computational efficiency.

The numerical procedure used to solve the transformed equations is an implicit finite-difference procedure similar to that of reference 25. The partial derivatives are replaced by linear-difference quotients. The result is a set of $N - 1$ linear algebraic equations for each of the unknown velocity components and enthalpy $\left(\bar{u}, \overline{w}, \text{ and } \overline{H}\right)$ at the N grid points for the next downstream station. The matrix for each set of these linear equations is tridiagonal, so that an efficient algorithm is used in their solution. After the solution for $\bar{u}$ and $\overline{w}$ is obtained from the momentum equations, the transformed normal velocity is obtained from the continuity equation; then the enthalpy (at each grid point) is obtained by the same numerical method used for $\bar{u}$ and $\overline{w}$. This procedure is repeated with updated values used in all difference coefficients until convergence is obtained.

The solutions were started at a small but finite chordwise distance from the stagnation line with an assumed set of profiles for $\bar{u}/u_e$, $\overline{w}/w_e$, and $\dfrac{\overline{H} - H_w}{H_e - H_w}$. This procedure was used for the present solutions because the correct limiting forms of the equations at $x = 0$ had not yet been incorporated in the computer program. It was found that consistent solutions for all variables could be obtained within a distance equivalent to 2 or 3 boundary-layer thicknesses by using a large number of small steps in the chordwise variable ξ. These solutions depended on the particular eddy-viscosity model used but were independent of the input profile shapes and input boundary-layer thicknesses, provided reasonable assumptions were used for these quantities.

The implicit finite-difference procedure as just described can provide, for all practical purposes, nearly "exact" solutions to the partial differential equations since the method is numerically stable. Of course, the accuracy of the solutions depends on the step sizes, the convergence criteria for the iterative cycles, and the accurate specification of boundary conditions. Essentially by trial-and-error processes, these matters

have been treated during the course of this and previous investigations (refs. 25 and 8) with the result that the present solutions are believed to be accurate to within 1 percent or better. Consequently, the comparison of theoretical predictions with data provides an indirect evaluation of the eddy-viscosity models, the mixing-length functions, and turbulent Prandtl number distributions since for a given set of boundary conditions, these are the only ingredients in the theory that can account for different predictions. Thus, by using various eddy-viscosity models and mixing-length functions in the theory and comparing results over a range of Reynolds number and with as many different experimental measurements as possible, the optimum formulation of Reynolds stress and turbulent Prandtl number can be determined. Such a process may be considered as "numerical experimentation" to determine the best form and values of the Reynolds stress.

EXPERIMENTAL METHODS

Experimental data have been obtained on a 60° swept slab with and without blowing at the blunt leading edge. The surface heat transfer, Mach number profiles, boundary-layer thickness, and surface streamlines were obtained for the model without blowing. For the model with blowing at the leading edge, the only data available are for surface heat transfer on the leading edge and downstream on the slab. The wind-tunnel facility and models will be described in detail in the following sections.

Facility

All the data presented herein were obtained in the Langley Mach 8 variable-density hypersonic tunnel. This blowdown-type facility has a contoured axisymmetric nozzle with an 18-inch-diameter test section. Transient testing techniques, that is, rapid exposure of models to established flow conditions, are accomplished by means of a model injection mechanism located directly beneath the test section. Windows are located on both sides and at the top of the test section for lighting and photographing models. The free-stream Mach number varies slightly with free-stream Reynolds number (ref. 26). Data will be presented herein for free-stream Reynolds numbers, based on leading-edge diameter, of 0.92×10^5, 2.6×10^5, and 9.3×10^5. The corresponding free-stream Mach numbers used in the data reduction are 7.81, 7.94, and 7.98. The stagnation temperatures are 1285° R, 1390° R, and 1475° R, respectively.

Models and Instrumentation

For this investigation the test configuration is a 60° swept slab with a leading-edge radius of 1/2 inch. One pressure model, three plastic heat-transfer models, and one porous-leading-edge model were used in the experimental tests. A sketch of the basic configuration used for the pressure model is shown in figure 1(b). The coordinate system

used to locate the instrumentation on the various models is also given in this figure. The forward portion of all models (ahead of the dashed lines) was geometrically identical with the pressure model shown. The aft portion of the plastic models and the porous-leading-edge model were modified as indicated by the dashed lines in the figure. The mounting plate as shown in the sketch was used for the pressure model and the plastic heat-transfer models. The mounting plate for the porous-leading-edge model was modified, as will be shown subsequently; however, the leading edge of the plate was 1/4 inch ahead of the apex of all models.

Pressure model.- The pressure model was made of stainless steel and was provided with seven chordwise rows of pressure orifices over a 12-inch span as shown in figure 2. The distribution of these orifices in the three chordwise rows used in this investigation is given in table I. A boundary-layer pitot-tube rake is shown attached to the model in figure 2. Details of the rakes used will be given in a subsequent section.

Phase-change heat-transfer models.- A photograph of one of the three plastic models used with the phase-change coating technique is shown in figure 3. The model shown was cast from an epoxy resin with a silica base. One of the other plastic heat-transfer models was cast from a slightly different mixture of epoxy and silica, and for the third model, mica was used as the base material. Therefore, these three models had different thermophysical properties. The value of the combination of these properties required in the phase-change method is $\sqrt{\rho c k}$. The values of this quantity for the three models were 0.073, 0.075, and 0.034 Btu/ft^2 $^\circ$R sec$^{1/2}$, respectively.

L-69-6073

Figure 2.- Pressure model.
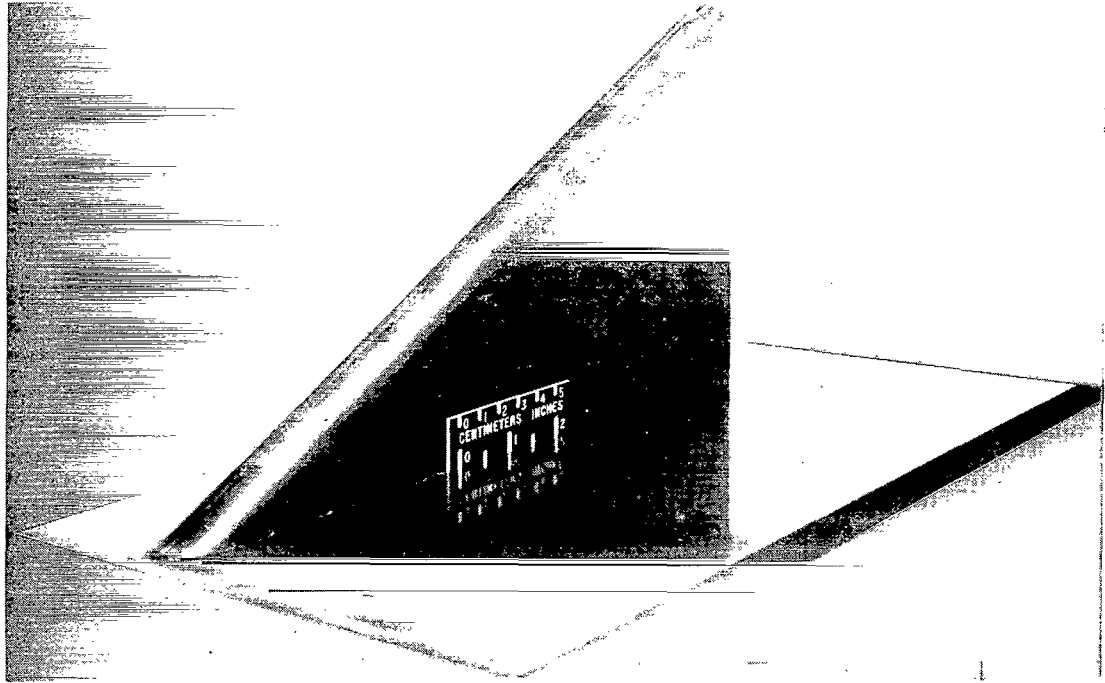
L-71-512

Figure 3.- Plastic model used with phase-change technique.

Porous-leading-edge model.- A photograph of the porous-leading-edge model used in this investigation is shown in figure 4. The leading edge of this model consisted of a porous hemicylinder $10\frac{1}{8}$ inches long and approximately 3/32 inch thick. The hemicylinder was made of sintered stainless steel with a porosity of approximately 13 percent. The leading edge was electron-beam welded to a swept slab which consisted of a machined, ribbed structure with a thin skin. The mounting-plate configuration for this model is different from that shown in figures 1(b), 2, and 3. In particular, the forward section of the plate was machined into an elliptical planform which projected beyond the periphery of the model apex by 1/4 inch.

The coolant air was fed into a chamber just behind the porous leading edge. The chamber could be pressurized to 415 psia. The pressure and temperature of the coolant air were measured in this chamber.

Thermocouples were installed in the porous leading edge and attached to the thin skin of the slab. The locations of the thermocouples used in this investigation are given in table II. To install the thermocouples on the porous leading edge, 0.016-inch-diameter balls were formed at the thermocouple junctions. Teflon-coated chromel-alumel wires of 0.003-inch diameter were used. The thermocouple wires were then inserted into a 0.013-inch-diameter hole which was burned by an electric-arc technique through the porous leading edge at an angle of 45° to the surface. The axes of the holes were alined

18

7.85 ≦ z/d ≦ 12.85

POROUS-LEADING-EDGE-
SOLID-SLAB INTERFACE

z
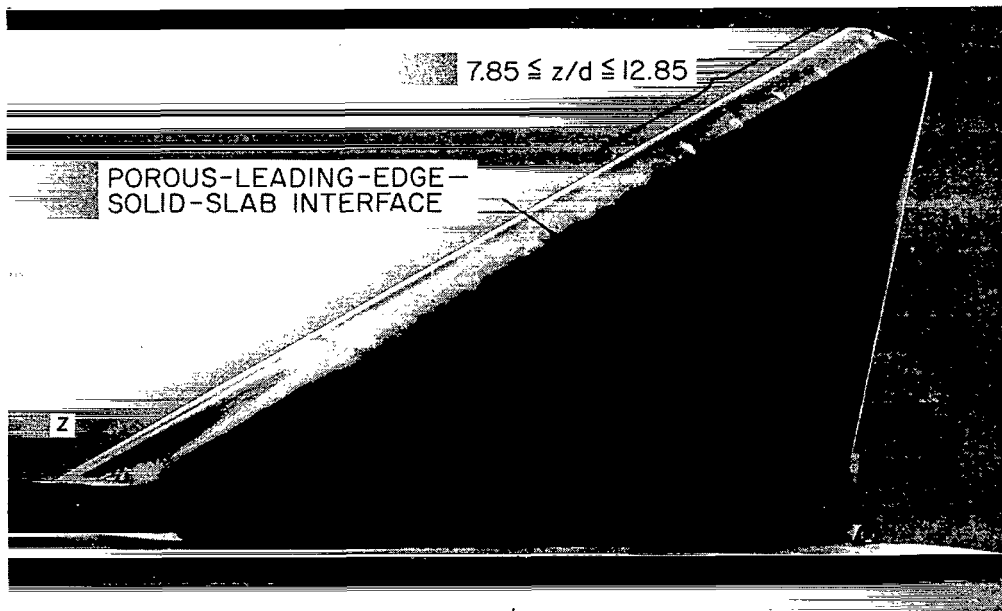
L-71-513

Figure 4.- Porous-leading-edge model.

in spanwise planes which in turn were normal to the surface. The thermocouple junction
(a 0.016-inch-diameter ball) was tapped into the 0.013-inch-diameter hole and finished
flush with the outer surface. The hole was then filled with epoxy resin to prevent direct
leaks of coolant air around the junction. This procedure resulted in a thermocouple junc-
tion within 0.004 inch of the external surface. Good thermal contact of the junction with
the porous matrix was obtained.

On the slab portion of the model the thermocouples were welded to the back surface
of the stainless-steel skin, which was 0.030 inch thick.

Boundary-layer pitot-tube rakes.- One of the boundary-layer pitot-tube rakes used
to obtain Mach number profiles is shown attached to the pressure model in figure 2. A
photograph of these rakes showing the tube assembly is presented in figure 5(a). The
rakes consisted of two rows of three pitot tubes each. Sketches of the pitot-tube con-
figurations with pertinent dimensions are given in figure 5(b).

Test Techniques and Data Reduction

All data were obtained by using a transient testing technique in which the tunnel
was started and brought to the desired operating conditions and then the model was rapidly
injected into the airstream by a pneumatic piston. An analog-to-digital data recording
system with a maximum resolution of 40 points per second was used for thermocouple and
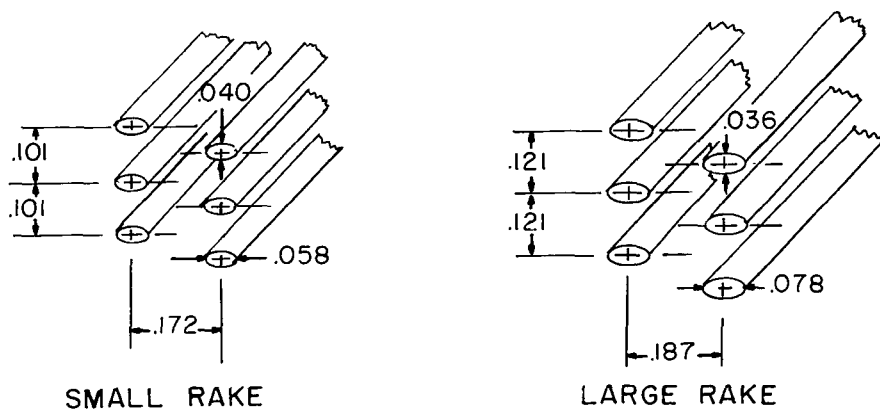static-pressure data.

19

LARGE RAKE
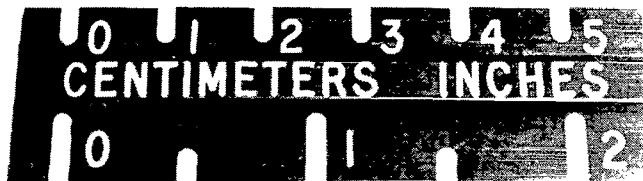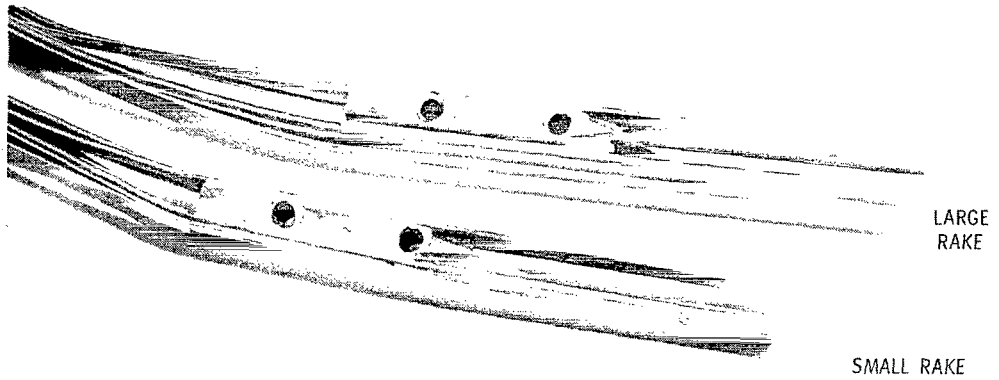
SMALL RAKE

L-69-7083.1

(a) Photograph of rakes.

SIZE OF ORIGINAL CIRCULAR TUBING

	I.D., in.	O.D., in.
SMALL RAKE	0.030	0.050
LARGE RAKE	.040	.060

SMALL RAKE

LARGE RAKE

(b) Sketches of pitot tubes. Dimensions are in inches.

Figure 5.- Pitot pressure rakes used for boundary-layer surveys.

Pressure data.- Strain-gage pressure transducers were used to measure the static pressures on the model shown in figure 2. The locations of the pressure orifices (0.040-inch diameter on the leading edge and 0.060-inch diameter on the slab) used in this investigation are given in table I. The output of the transducers was monitored to determine when time-steady pressures were reached, then the data were recorded on the readout system at the rate of 20 points per second.

The pitot-tube rakes shown in figure 5 were mounted on the pressure model as indicated in figure 2. Pitot-pressure data were obtained at five chordwise locations on the slab portion of the model. The rakes were alined so that the pitot tubes were parallel to the free-stream flow direction. The plane of the pitot orifices was located approximately 1/4 inch behind a static-pressure orifice at each chordwise location. The y-location of the tube assembly was adjusted with shims between the rake and model. The pitot-pressure data were read from photographs of a mercury manometer board.

The ratios of the local surface static pressure to the pitot pressure were used to compute the Mach number distributions through the boundary layer. The boundary-layer thickness was taken as the distance from the surface where the Mach number became approximately constant.

Oil flow.- In order to obtain the direction of the wall streamlines and the overall flow pattern, small dots of a mixture of oil and lampblack were placed on the slab portion of the pressure model. The model was then rapidly injected into the airstream. After exposure to the flow of 3 to 8 seconds, depending on the Reynolds number, the model was retracted and the resultant patterns photographed.

Heat transfer for no blowing.- Heat-transfer-coefficient distributions on the plastic "stycast" models (fig. 3) were obtained with the phase-change coating technique (ref. 27). In this technique, a thin surface coating of material that undergoes a visible phase change at a known temperature is sprayed on the model. The model is then injected rapidly into the established flow and the phase-change patterns which develop as the model is heated are recorded by motion-picture photography. The patterns of isothermal lines so obtained may be transformed to lines of constant heat-transfer coefficient provided the distribution of adiabatic wall temperature is available and the thermophysical properties (ρck) of the model material are known. Exact solutions of the heat-conduction equation for the specific geometry are not generally practical; therefore, the local heat-transfer coefficients for the model are determined from the solution for a semi-infinite slab. The results obtained with this assumption are a good approximation to the solution for the actual body geometry when the depth of heat penetration is small compared with pertinent model dimensions, as is the case for the present model. A detailed discussion of the accuracy limits due to the semi-infinite-slab assumption is presented in reference 27.

<u>Test procedure for heat transfer with blowing</u>.- The porous-leading-edge model described previously and shown in figure 4 was instrumented to provide heat-transfer data on both the porous leading edge and on the thin-skin slab. The locations of the thermocouples used in the present investigation are given in table II.

For the wind-tunnel tests, the desired mass flow rate was established first with the model in the retracted position inside the sealed chamber below the tunnel test section. (See ref. 20.) During the tunnel startup process this chamber was evacuated to tunnel static pressure which was about 0.05 times the pressure on the stagnation line of the swept leading edge after the model was exposed to the flow. This sudden change in external pressure on the porous leading edge after model injection did not affect the preset mass flow because of the large pressures (150 to 400 psig) inside the model.

Heat-transfer data were used during the period from 0.2 to 1.5 seconds after the model first entered the airstream. Because of the short testing time, the model was practically isothermal; thus heat-conduction effects were minimized and any change in the injected mass flow rate which would occur with an increase in model temperature (eq. (36)) was minimized. The thermocouple data were recorded at a rate of 20 points per second on the digital readout system.

<u>Data reduction procedures for tests with blowing</u>.- A numerical procedure was developed to reduce the temperature-time histories of each thermocouple within the porous wall to heating rates. The method provides an approximate solution of the two-dimensional heat-conduction problem in a porous matrix with one-dimensional (or radial) fluid flow and with temperature-dependent thermal properties. The temperature of the fluid is assumed to be the same as that of the porous matrix. Details of this procedure and the manner in which it was applied to the porous-leading-edge model are given in appendix A.

Downstream of the interface of the porous leading edge and the slab, the thermo-couple wires were spotwelded to the inside surface of the thin stainless-steel skin which was 0.030 inch thick. Here, the heating rates were obtained by fitting a second-degree curve to the temperature-time data by the method of least squares, over a time interval of 1.0 second. The time derivatives of temperature were then computed from the slopes of these second-degree curves at the midpoint of the 1.0-second time interval. The heating rates, neglecting conduction, were then obtained from the equation

$$\dot{q}_w = (\rho c)_m \, \Delta y \, \frac{dT_w}{dt} \tag{27}$$

RESULTS AND DISCUSSION

Static Pressure Distribution

The experimental pressure distributions obtained with the model of figure 2 are shown in figure 6. The line faired through the data was used as the distribution of p_e from which u_e and ρ_e were computed for the input to all theoretical solutions included herein. An isentropic expansion from p_s to p_e was assumed for these computations of u_e and ρ_e.
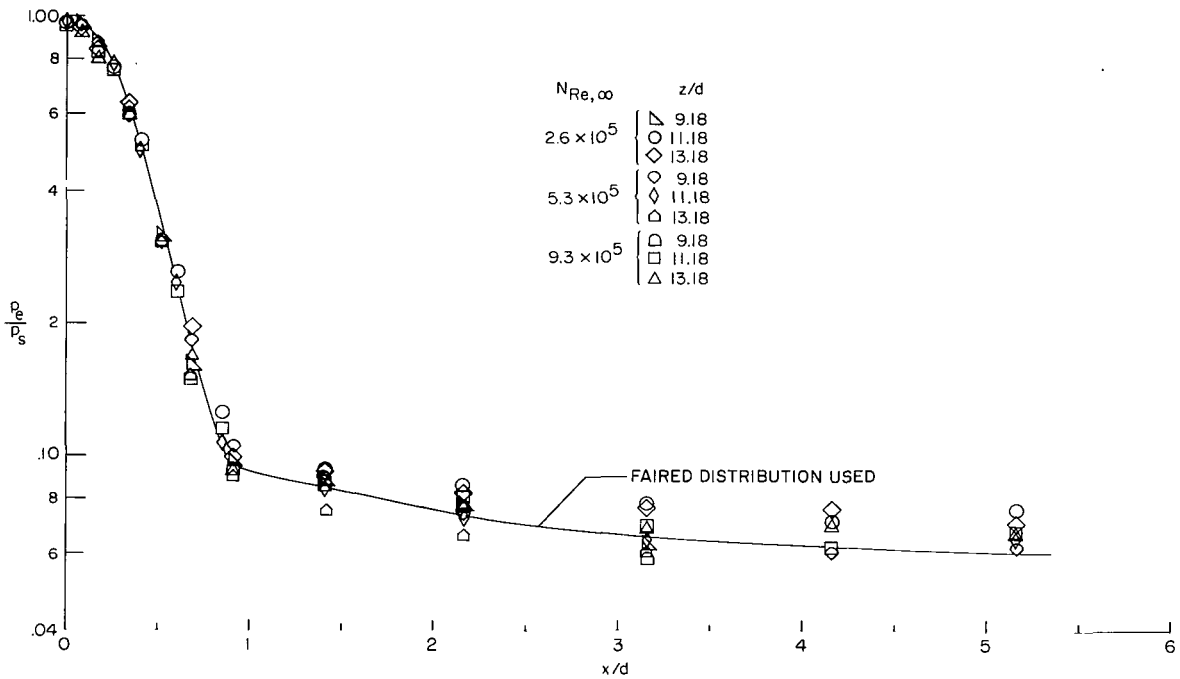

Figure 6.- Chordwise distribution of static pressures.

Zero Blowing

Heat transfer.- The chordwise distribution of heat-transfer coefficient at the spanwise station $z/d = 10.6$ for $N_{Re,\infty} = 0.92 \times 10^5$ is presented in figure 7. The plastic models (fig. 3) were used to obtain these data with the phase-change technique. The width of the hatched band represents the scatter in 56 data points obtained with eight different phase-change coatings $\left(0.45 \leqq T_w/T_t \leqq 0.55\right)$ on the three models with different thermophysical properties. The theoretical laminar distribution (solid line) was obtained with the finite-difference procedure for $T_w/T_t = 0.4$ and $\epsilon = 0$. The good agreement between experimental data and the theoretical predictions indicates that the numerical
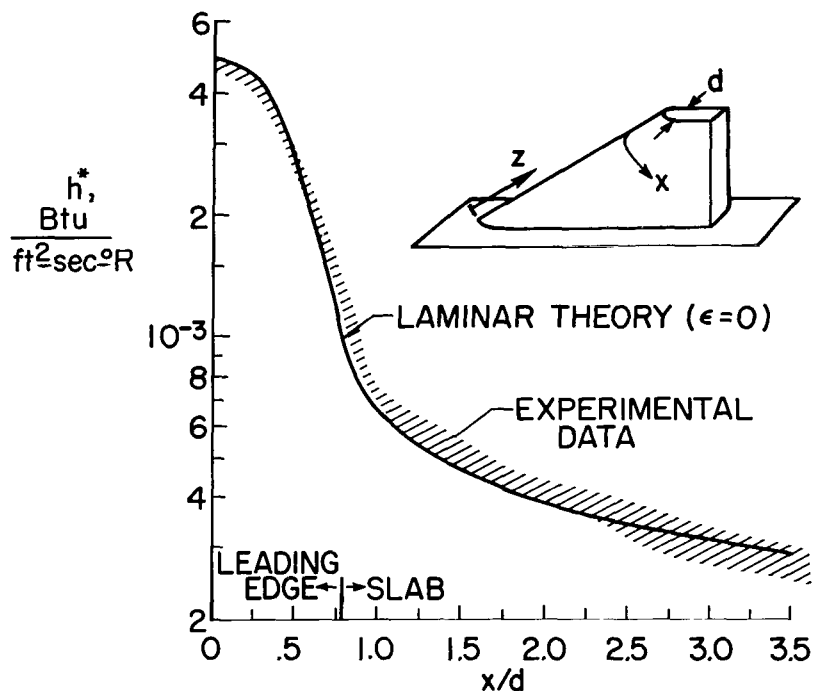
Figure 7.- Comparison of theory and data for laminar flow.
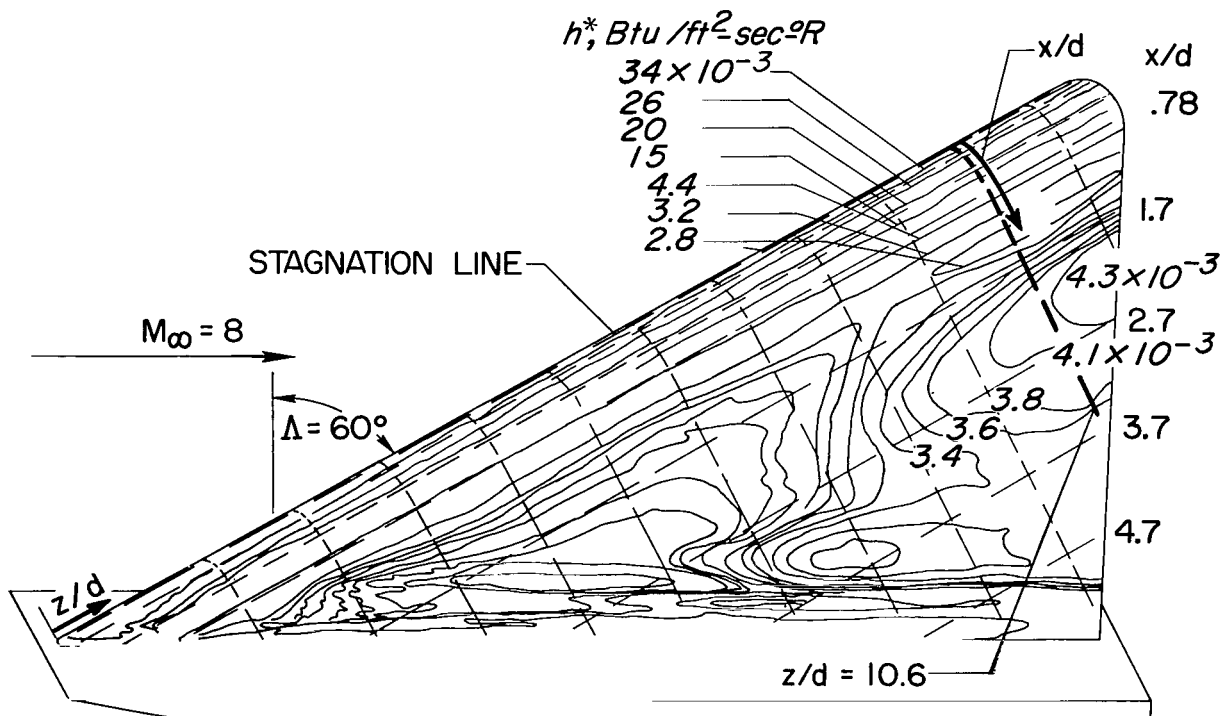$N_{Re,\infty} = 0.92 \times 10^5$; $\dot{m} = 0$; $z/d = 10.6$.

procedure satisfactorily predicts the experimental heat transfer and that the leading-edge boundary layer is laminar at this Reynolds number in agreement with the criteria of reference 28.

Heat-transfer-coefficient contours obtained for typical runs on the plastic models with the phase-change coating technique are shown in figures 8(a) and 8(b) for $N_{Re,\infty} = 2.6 \times 10^5$ and 9.3×10^5, respectively. In figure 8(a) the values of h^* decrease continuously along the chord at $z/d = 10.6$. The fact that the contours in this region are essentially parallel to the leading edge indicates that the interference disturbances between the mounting plate and the model are small; thus, the infinite-cylinder approximation is acceptable.

In contrast to the contours in figure 8(a), the contours at the larger Reynolds number (fig. 8(b)) are not parallel to the leading edge at any spanwise station for $x/d \gtrsim 1.2$. On the leading edge for $x/d \lesssim 1.0$ and along the chord $z/d = 10.6$, the contour lines are parallel to the stagnation line and the values of h^* decrease with increasing x/d. However, for $x/d \gtrsim 1.3$ (at $z/d = 10.6$) the values of h^* increase from a minimum of 2.8×10^{-3} to a maximum of 4.3×10^{-3}. At $x/d \approx 2.2$, the values of h^* again begin to decrease. The locations of these minimum and maximum contours in h^* are too far from the mounting plate to be caused by interference effects, as indicated by the results of figure 8(a). Oil-flow patterns, to be presented subsequently, substantiate the lack of

24

h^*, Btu/ft^2-sec-$^\circ R$

11.9×10^{-3}
7.8
4.5
2.2

STAGNATION LINE

$M_\infty = 8$

$\Lambda = 60^\circ$

x/d

x/d
.78
1.7
2.7
3.7
4.7

1.5
1.2
1.0
$.88$
$.77$
$.67$

$.77$

2.2

z/d

z/d = 10.6

(a) $N_{Re,\infty} = 2.6 \times 10^5$.

h^*, Btu/ft^2-sec-$^\circ R$

34×10^{-3}
26
20
15
4.4
3.2
2.8

STAGNATION LINE

$M_\infty = 8$

$\Lambda = 60^\circ$

x/d

x/d
.78
1.7

4.3×10^{-3}
2.7
4.1×10^{-3}
3.8
3.6
3.4

3.7

4.7

z/d

z/d = 10.6
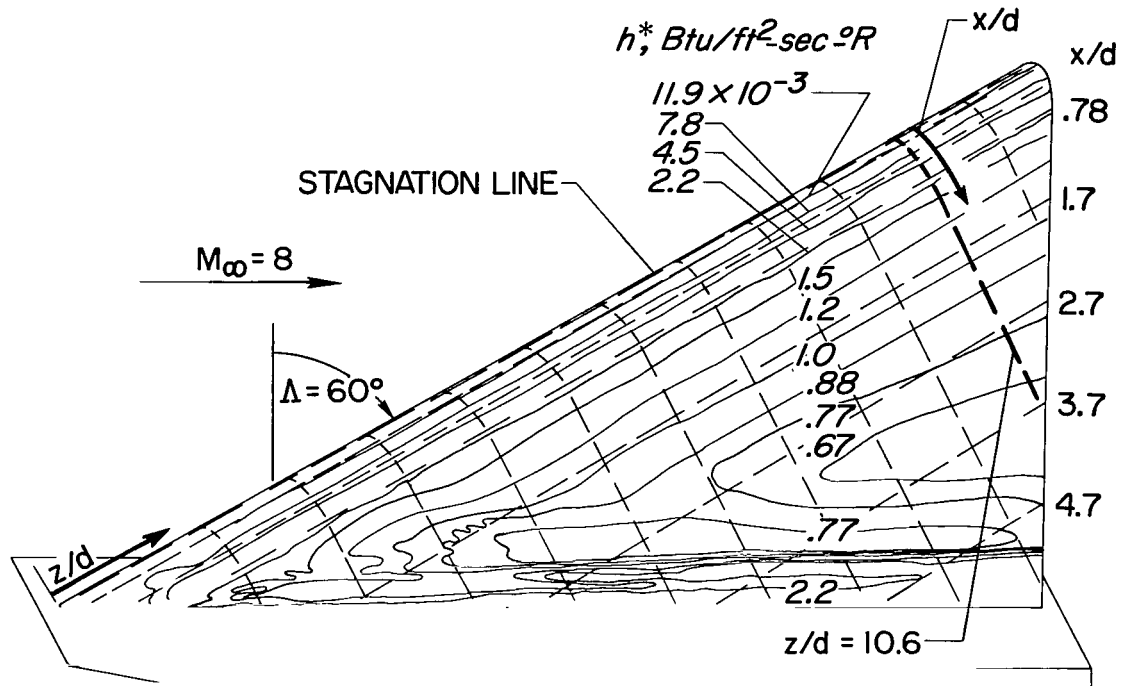
(b) $N_{Re,\infty} = 9.3 \times 10^5$.

Figure 8.- Test configuration showing heat-transfer-coefficient contours for $\dot{m} = 0$.

plate interference effects in this region. Figure 8(a) also shows that the effects of the truncated end of the slab are not responsible for the contour behavior noted in figure 8(b).

Comparisons and discussion of these different results are best made by means of heat-transfer-coefficient distributions. The chordwise distributions of h^* along the chord $z/d = 10.6$ for the same test conditions of figure 8 are given in figure 9. Theoretical predictions made with the two eddy-viscosity models described previously (one corresponding to the assumptions of invariant turbulence and the other to Lettau's (ref. 10) vorticity-transfer hypothesis) for $T_w/T_t = 0.4$ and $(l/\delta)_{max}$ of 0.05 and 0.07 are shown as the dashed lines in figure 9. The solid lines of figure 9 represent predictions of the laminar theory obtained with $\epsilon = 0$.

The data and theoretical results in figure 9(a) are for $N_{Re,\infty} = 2.6 \times 10^5$. The width of the hatched band represents the scatter in 97 data points obtained with six different phase-change coatings $\left(0.41 \leqq T_w/T_t \leqq 0.58\right)$ on the three models with different values of ρck. Reference 29 presents comparisons of experimental and theoretical heat-transfer results which indicate that the leading-edge boundary layer is turbulent at this Reynolds number. In figure 9(a) the two theoretical turbulent distributions $\left(\text{different values of } (l/\delta)_{max}\right)$ are within the spread of the experimental data in the leading-edge region. The original density of data points for the band shown in this figure indicates that the agreement of experimental data and predictions from the finite-difference procedure is best when the $(l/\delta)_{max}$ value of 0.05 is used. On the forward portion of the slab $(0.785 \leqq x/d \lessgtr 1.5)$, the experimental values of h^* fall below the theoretical turbulent distribution and approach the laminar predictions. The experimental values of h^* remain slightly above the laminar predictions over the remainder of the slab region to $x/d = 3.5$.

The experimental and theoretical results for $N_{Re,\infty} = 9.3 \times 10^5$ are shown in figure 9(b). On the leading edge the theoretical turbulent prediction with the invariant-turbulence assumption and $(l/\delta)_{max} = 0.05$ is in best agreement with the data. On the forward portion of the slab, the data again drop below the turbulent predictions and tend to approach the laminar prediction. However, in contrast with the experimental results at the lower Reynolds number (fig. 9(a)), the level of the data begins to increase at $x/d \approx 1.3$ until agreement with turbulent levels is obtained at $x/d \approx 2.0$.

These trends of the experimental data with x/d and Reynolds number (figs. 9(a) and 9(b)) as compared with the theoretical predictions suggest the possibility of laminarization of the initially turbulent boundary layer on the leading edge. The drop in experimental heat transfer just aft of the rapid expansion on the leading edge until nearly laminar values are reached could also be caused partly by the effect of streamline curvature on the mixing length. (See refs. 14 and 30.) However, if the effects of curvature were the main cause of this drop in heating, it might be expected that the experimental
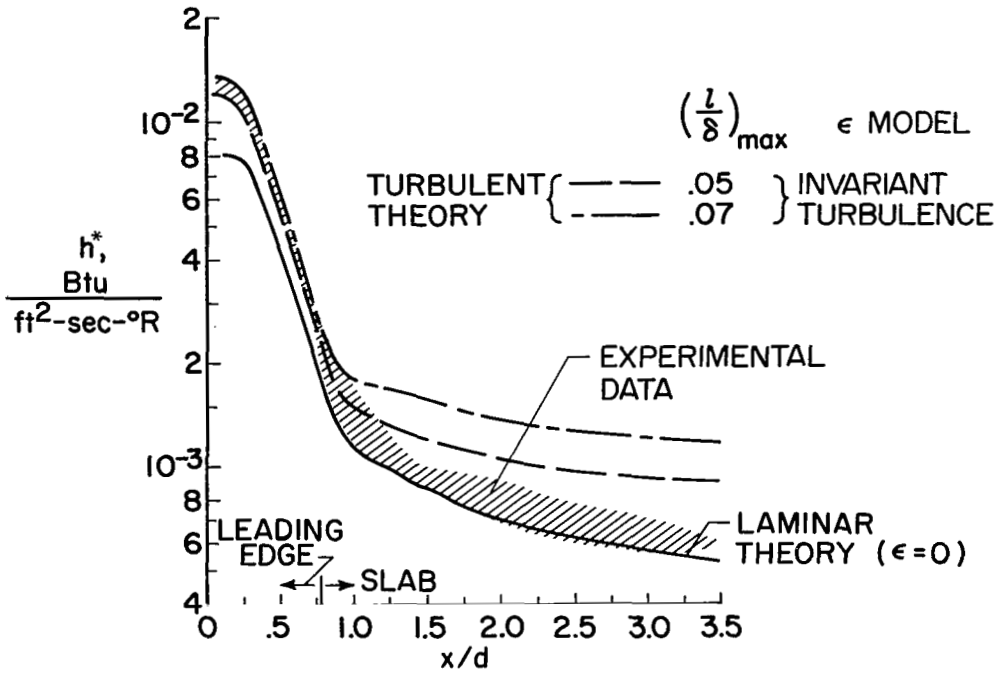
(a) $N_{Re,\infty} = 2.6 \times 10^5$.
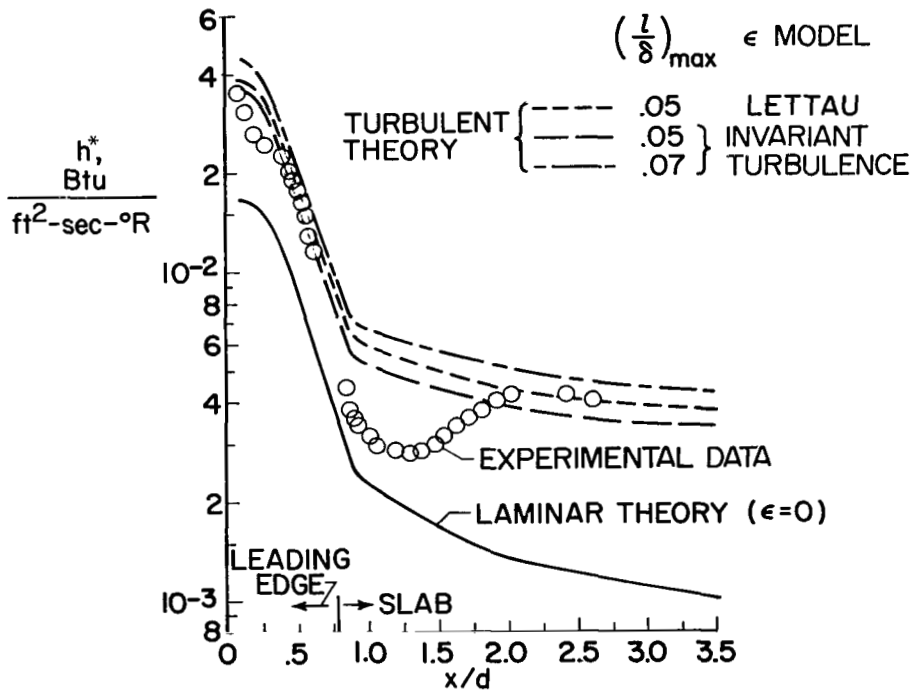
(b) $N_{Re,\infty} = 9.3 \times 10^5$.

Figure 9.- Chordwise distribution of heat-transfer coefficient. $\dot{m} = 0$; $z/d = 10.6$.

levels of heating on the slab would rapidly approach turbulent values at both Reynolds numbers since the curvature on the slab is zero. The possibility of laminarization will be discussed further after additional data are presented that will confirm the experimental trends noted in figure 9.

Surface streamlines.- Oil-flow patterns obtained on the slab portion of the pressure model at $N_{Re,\infty} = 2.6 \times 10^5$ and 9.3×10^5 are shown in figures 10(a) and 10(b), respectively. The streamlines at the wall computed from theoretical values of $\tau_{w,x}$ and $\tau_{w,z}$ for both laminar and turbulent flow are included in the figure for comparison. These results are referred to in the figures as "surface viscid" streamlines. Inviscid streamlines at the edge of the boundary layer as based on the pressure distribution of figure 10 and the infinite-cylinder assumption that $\overline{w}_e$ is constant are also shown. The large deviations between the viscid and inviscid streamlines indicate that large cross flows are present.

For the lower Reynolds number (fig. 10(a)), the oil-flow patterns are essentially parallel to the laminar viscid streamline. This result is in agreement with the heat-transfer trends noted in figure 9(a). At $N_{Re,\infty} = 9.3 \times 10^5$ (fig. 10(b)), the oil-flow patterns are nearly parallel (except just aft of the leading edge) to the theoretical viscid streamline for turbulent flow with the invariant-turbulence eddy-viscosity model. Again these results are in agreement with the corresponding trends of figure 9(b). Surface oil-flow patterns caused by the boundary-layer pitot-tube rake are evident in figure 10(b). Of course, these interference patterns and those near the mounting plate should be disregarded in the comparisons with theoretical predictions.

Velocity and Mach number profiles.- In order to illustrate the behavior of the velocity and stagnation-temperature profiles obtained from the finite-difference solutions, the profile parameters $\bar{u}/u_e$, $\overline{w}/w_e$, and $\dfrac{\overline{T}_t - T_w}{T_{t,e} - T_w}$ are plotted against y/δ in figure 11. These profiles are in the stagnation region ($x/d \approx 0.1$) for the two Reynolds numbers of 2.6×10^5 and 9.3×10^5.

The chordwise velocities "overshoot" the values of u_e appreciably for $y/\delta \gtrless 0.3$. These results are qualitatively similar to those of reference 11 where exact solutions for the laminar compressible boundary layer on swept cylinders also resulted in overshoot of the chordwise velocity profiles. In reference 11 the overshoot phenomenon was attributed to the effects of compressibility. Comparison of the computed profiles with a power-law profile
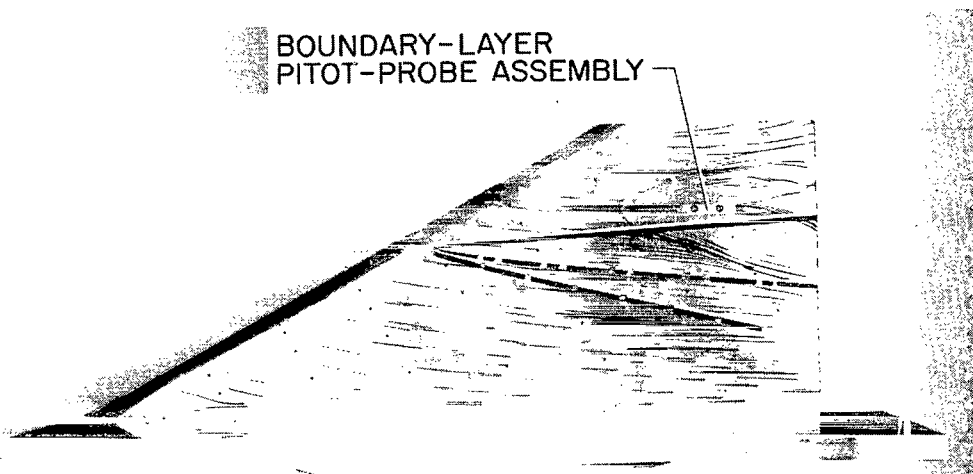
$$\left.\begin{array}{c} \dfrac{\bar{u}}{u_e} \\[2mm] \dfrac{\overline{w}}{w_e} \end{array}\right\} = \left(\dfrac{y}{\delta}\right)^n \tag{28}$$
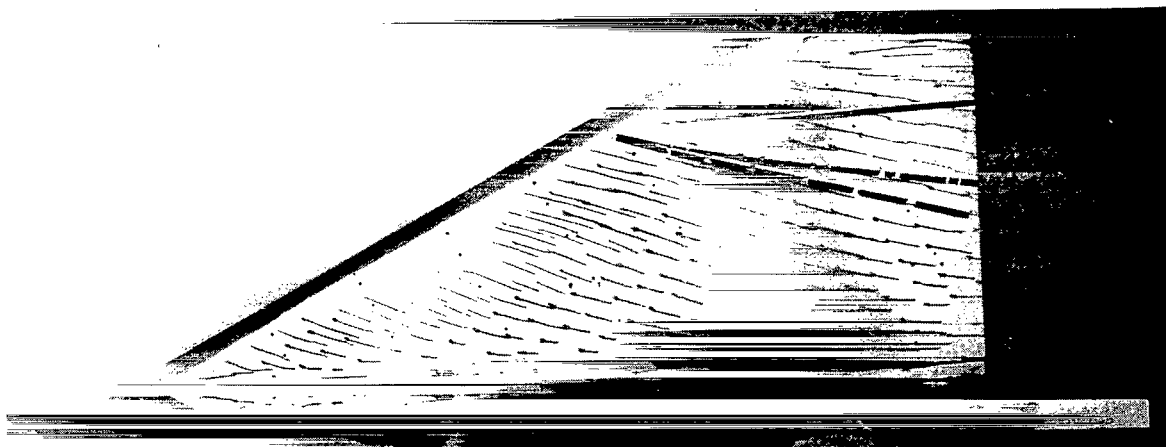
(a) $N_{Re,\infty} = 2.6 \times 10^5$.

(b) $N_{Re,\infty} = 9.3 \times 10^5$.

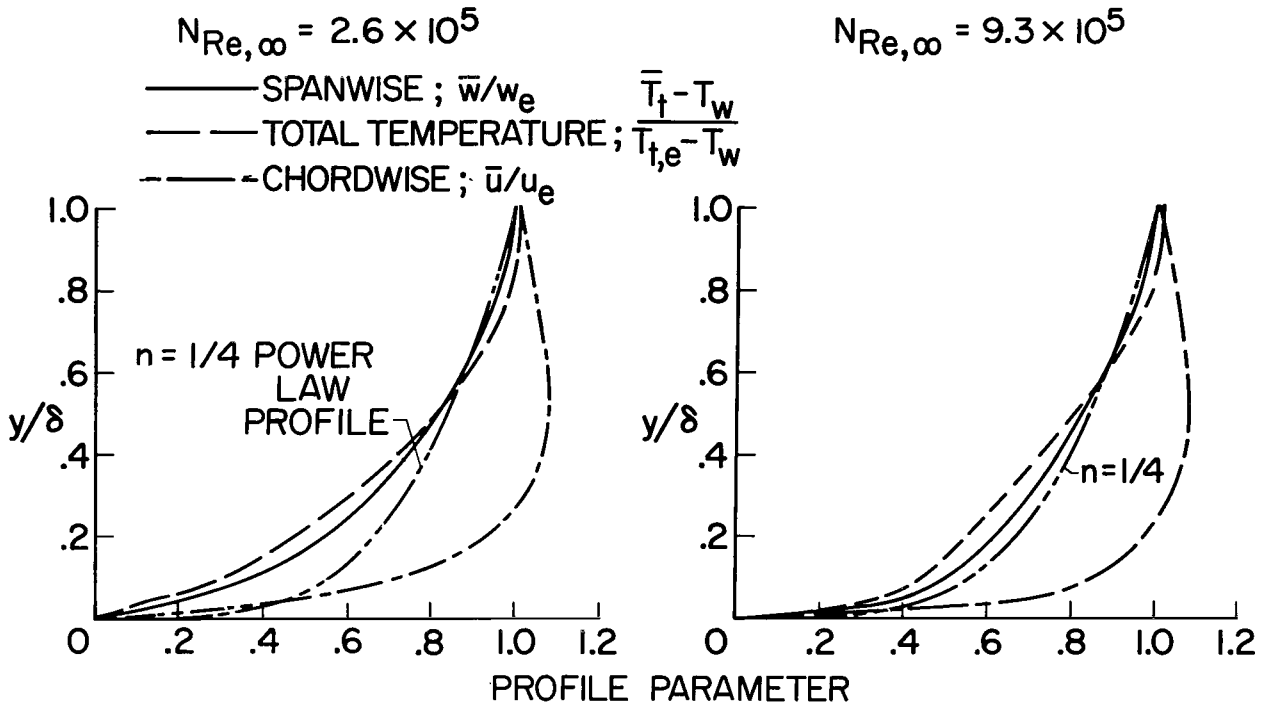Figure 10.- Comparisons of computed streamlines with surface oil-flow lines for $\dot{m} = 0$.

Figure 11.- Computed profiles in stagnation region $x/d \approx 0.1$. $\dot{m} = 0$.

for $n = 1/4$ also shown in figure 11 indicates that the present results differ greatly from simple power-law profiles, as used for example in reference 3.

Experimental and theoretical Mach number profiles are shown in figures 12(a) and 12(b) for the test Reynolds numbers of 2.6×10^5 and 9.3×10^5. The experimental Mach number profiles were obtained from the ratios of measured pitot pressures and the local static pressures given by the faired line in figure 6. The theoretical profiles were computed for laminar ($\epsilon = 0$) and turbulent flow. The invariant-turbulence model with $(l/\delta)_{max} = 0.05$ was used in the turbulent calculations.

Although there is considerable scatter in the data, comparisons at the lower Reynolds number (fig. 12(a)) indicate good agreement between the experimental results and predicted profile shapes and boundary-layer thicknesses for laminar flow. At the higher Reynolds number (fig. 12(b)) the experimental results are in excellent agreement with the predictions for turbulent flow. The pitot-pressure data are therefore consistent with the results of figures 9 and 10 which showed that for $x/d > 2.0$, the boundary layer was nearly laminar at the lower Reynolds number and turbulent at the higher Reynolds number.

Boundary-layer thickness.- The boundary-layer-thickness distributions with x/d for $N_{Re,\infty} = 2.6 \times 10^5$ and 9.3×10^5 are shown in figures 13(a) and 13(b). The bars
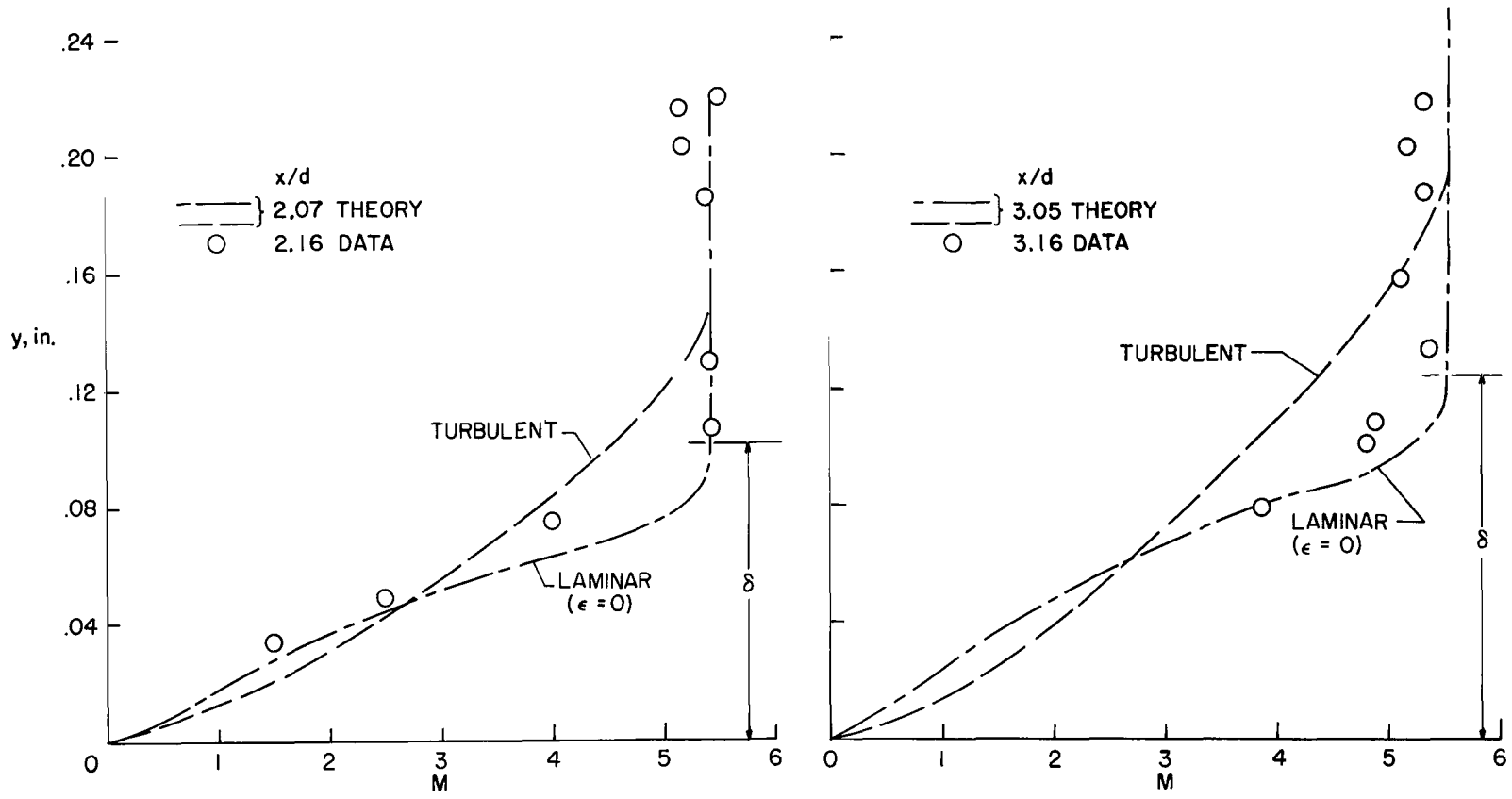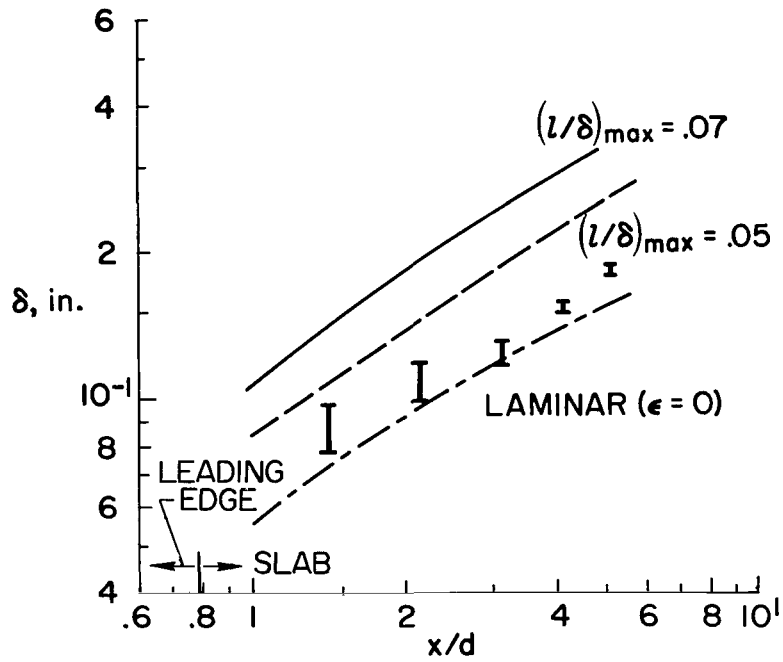
(a) $N_{Re,\infty} = 2.6 \times 10^5$.

Figure 12.- Mach number profiles. All computed profiles for turbulent flow were obtained with the invariant-turbulence model and $(l/\delta)_{max} = 0.05$. $\dot{m} = 0$.
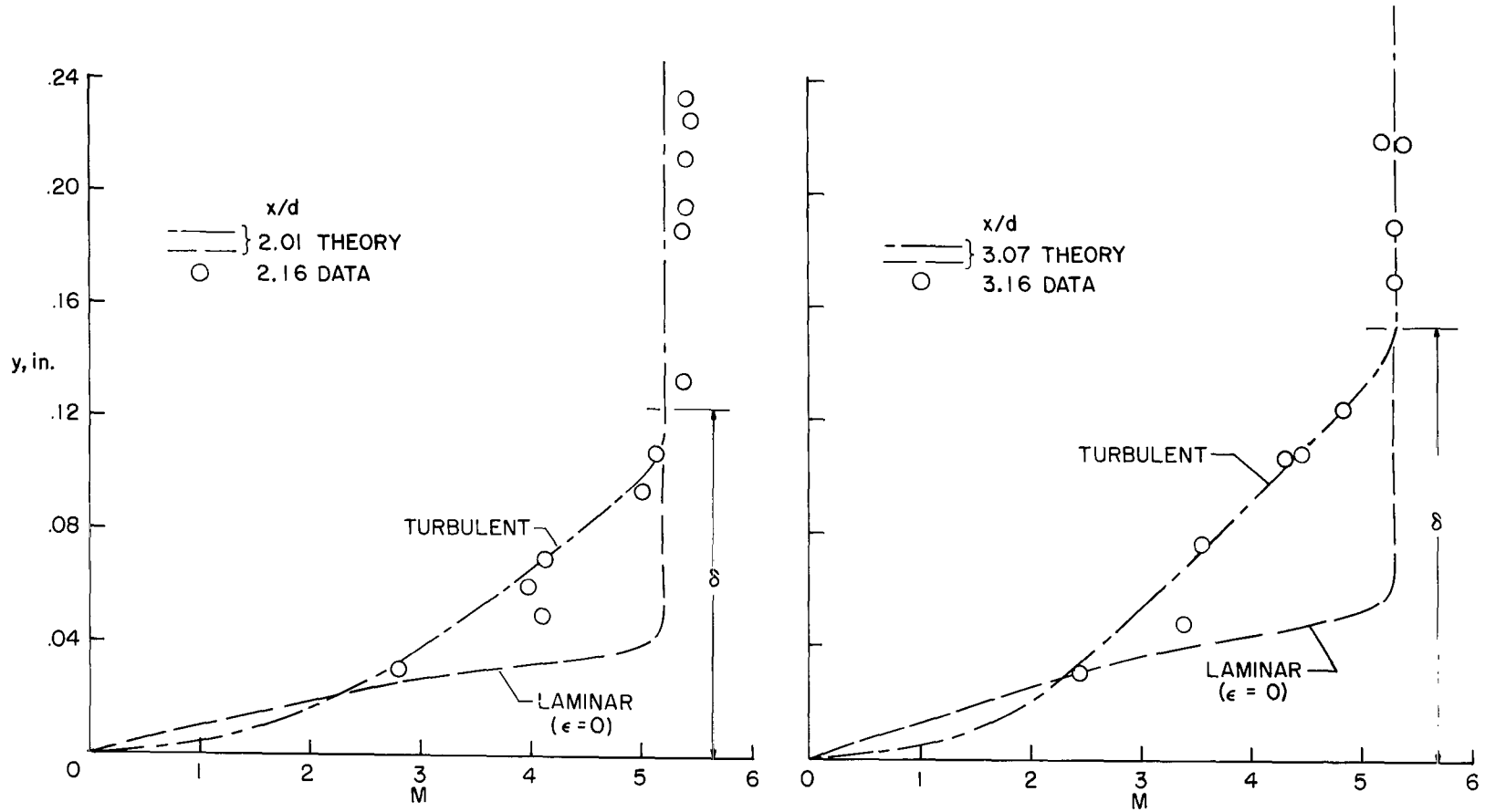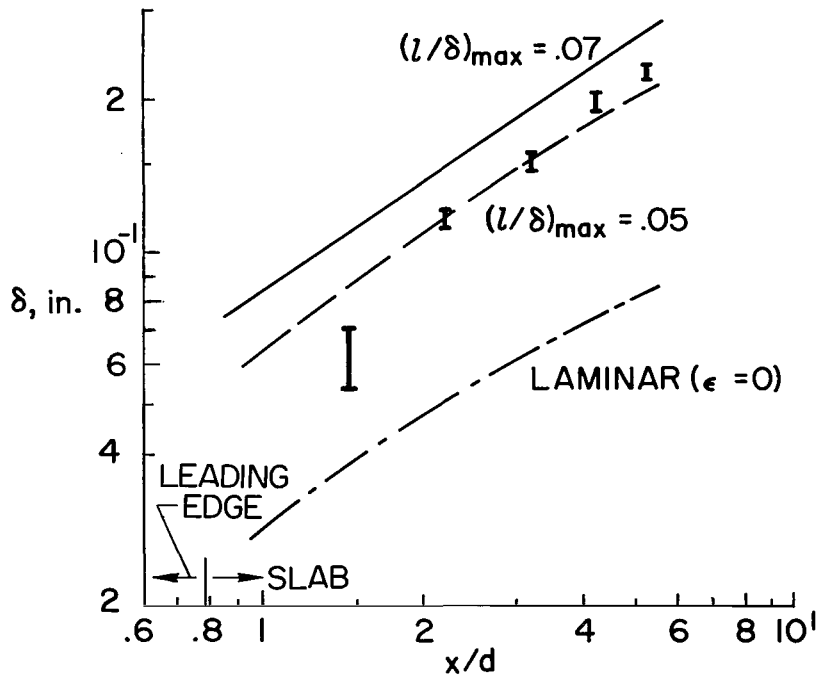
(b) $N_{Re,\infty} = 9.3 \times 10^5$.

Figure 12.- Concluded.

(a) $N_{Re,\infty} = 2.6 \times 10^5$.

(b) $N_{Re,\infty} = 9.3 \times 10^5$.

Figure 13.- Chordwise distribution of boundary-layer thickness for $\dot{m} = 0$ and $z/d = 10.6$. Invariant-turbulence model used for the two upper lines. Bars indicate experimental data spread.

indicate the spread in the experimental data. The values of boundary-layer thickness were obtained from the Mach number profiles as indicated for typical data in figure 12. In figure 13(a) the first data point at $x/d = 1.41$ is between the lower turbulent prediction and the laminar prediction. As x/d increases, the experimental values of δ approach the laminar predictions up to $x/d \approx 3.2$, in agreement with the results of the heat-transfer and oil-flow data (figs. 9(a) and 10(a)). The last two data points at $x/d = 4.16$ and 5.16 show a slight increase from the theoretical laminar values. Since the heat-transfer data of figure 9(a) only extended to $x/d = 3.5$, any trends for $x/d > 3.5$ in the heating data are not available. Close examination of the oil-flow data (fig. 10(a)) indicates a slight upward trend near the end of the slab ($x/d \approx 5$) toward the turbulent prediction. However, this trend may be caused partly by interference from the mounting plate.

At the larger value of $N_{Re,\infty}$ (fig. 13(b)), the first data point for boundary-layer thickness ($x/d = 1.41$) is between the laminar and turbulent distributions. This result is again consistent with the corresponding heat-transfer and oil-flow results of figures 9(b) and 10(b). The remaining data points are on or slightly above the turbulent result with $(l/\delta)_{max} = 0.05$ and are also consistent with the heat-transfer and oil-flow data.

Laminarization.- Comparisons of experimental and theoretical heat-transfer results presented herein indicate that the boundary layer on the leading edge of the 60° swept slab is turbulent for both $N_{Re,\infty} = 2.6 \times 10^5$ and 9.3×10^5. These indications are consistent with those presented in reference 29.

The preceding comparisons of data and theory on the slab ($x/d > 0.78$) for heat transfer, oil flow, Mach number profiles, and boundary-layer thickness have all given consistent results regarding the apparent trends toward laminar or turbulent flow. To provide some further indication of whether these trends were caused by laminarization of the initially turbulent boundary layer as the flow expands around the leading edge, values of a laminarization parameter have been computed. This parameter is based on the form proposed in references 31 and 32 but modified herein for application to three-dimensional flow.

The investigations in references 31 and 32 for conical nozzle flow showed that laminarization effects become significant when

$$\frac{\mu_e}{\rho_e \bar{u}_e^2} \frac{d\bar{u}_e}{dx} \gtrsim 2 \times 10^{-6} \tag{29}$$

This parameter can presumably be extended to three-dimensional flow by using streamline coordinates. That is, by replacing $\bar{u}_e$ with $\bar{q}_e$ and dx with ds, the value for the parameter of 2×10^{-6} would be applicable to three-dimensional flow. Thus, when

$$\frac{\mu_e}{\rho_e \bar{q}_e^2} \frac{d\bar{q}_e}{ds} \gtrsim 2 \times 10^{-6} \tag{30}$$

laminarization in three-dimensional flows might be expected if the same mechanisms are responsible for the phenomenon as in two-dimensional flow. However, calculated values of the parameter in relation (30) for the present configuration were at most nearly 1 order of magnitude smaller than 2×10^{-6}. Apparently, if the tendency noted in the present results for the heat transfer to approach laminar values aft of the leading edge were caused by laminarization effects, the criterion of relation (30) would be much smaller. A possible explanation of a smaller criterion in three-dimensional flow is as follows: It has been established that three-dimensional laminar boundary layers with large cross flows are inherently unstable and therefore premature transition due to small disturbances is likely. (See ref. 33.) For the present configuration, disturbances generated by the leading-edge portion of the mounting plate upstream of the model apex would be sufficient to cause transition to turbulent flow at small Reynolds numbers. (See refs. 28 and 34.) Consequently, the turbulent boundary layers indicated on the leading edge in the present tests may have low levels of turbulence intensity and would therefore be highly susceptible to laminarization. The small values of $(l/\delta)_{max}$ used in the theory (0.05 compared with usual values of approximately 0.09) tend to support the possibility of low turbulence levels, since small values of the mixing length cause small values of eddy viscosity which imply low levels of turbulence.

Heat Transfer With Blowing

Blowing-rate distribution on porous leading edge.- The mass-injection-rate distribution on the surface of the porous leading edge is given in figure 14 in the form of the permeability parameter α. This parameter would be constant if the porous material were perfectly uniform in porosity and thickness. The chordwise variation in permeability is shown in figure 14(a) for the spanwise location $z/d = 8.85$ and for the range of internal pressures shown. The spread of the data at a given x/d location in this figure gives an indication of the repeatability of the calibration technique, since the only variable was the internal pressure. The chordwise variation of the permeability for a range in span of 4 inches $(7.85 \leq z/d \leq 11.85)$ and pressures of 250 and 300 psig is presented in figure 14(b). The data spread here is due primarily to the spanwise variation in the permeability. The technique used to measure the mass injection rates is described in appendix B.

Application of theory for nonsimilar blowing rates.- The present finite-difference procedure can be applied directly to calculation of boundary layers with surface mass transfer if the chordwise distribution of the normal velocity v_w at the surface is known.
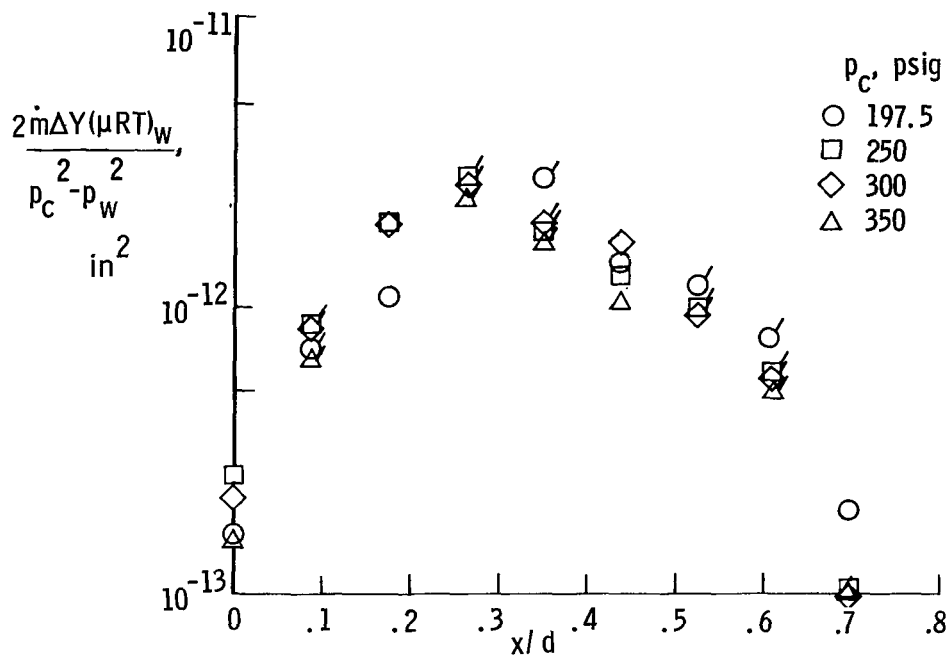
(a) $z/d = 8.85$ and various values of p_c.
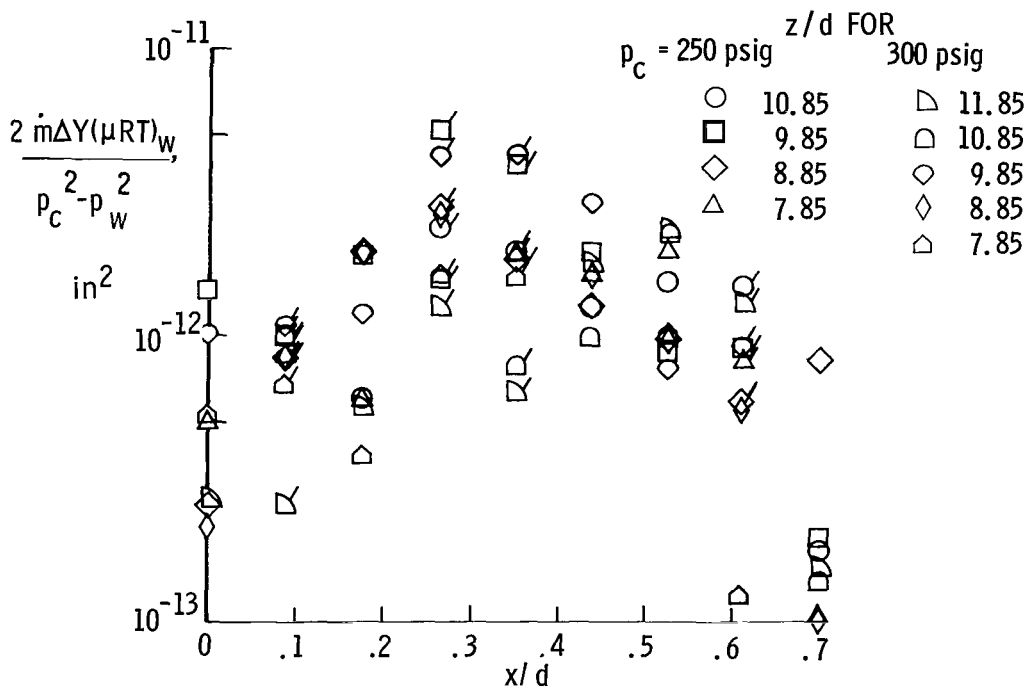
(b) $7.85 \lesssim z/d \lesssim 11.85$; $p_c = 250$ and 300 psig.

Figure 14.- Chordwise distributions of permeability on porous leading edge. (Flagged symbols indicate data "folded" from negative x/d locations.)

The infinite-cylinder condition that spanwise derivatives of all mean-flow quantities are zero requires that $\frac{\partial v_w}{\partial z} = 0$. This requirement is not met in the present tests because of the large spanwise variations in the permeability α as shown by figure 14(b). Equation (36) in appendix B shows that the spanwise variations in v_w are directly proportional to the α variations, since $\frac{\partial p_w}{\partial z} \approx 0$.

Consequently, a direct comparison of theoretical predictions with data is not possible. Instead, calculations pertaining to a given value of p_c for each of the two values of $N_{Re,\infty}$ have been carried out for two different blowing-rate distributions that represent the maximum and minimum range of α values over the span interval $7.85 \leq z/d \leq 12.85$. These results will then be compared with the experimental data over the same span interval. Thus the general validity of the theoretical predictions can be assessed, provided that the experimental values of heat transfer on both the porous leading edge and the downstream slab are affected mainly by leading-edge blowing rates within the same span interval.

The chordwise distributions of the maximum and minimum mass flow measured over the span interval $7.85 \leq z/d \leq 12.85$ are shown in figure 15 as the hatched bands for values of the internal chamber pressure of 212, 300, and 405 psia. The chordwise distributions of v_w, corresponding to these maximum and minimum mass flow rates, were used as inputs for the computer program. Solutions for these input flow rates were then obtained for laminar flow ($\epsilon = 0$) and turbulent flow where the invariant-turbulence or the Lettau eddy-viscosity model with $(l/\delta)_{max} = 0.05$ was used. Comparisons with experimental heat-transfer data for the two test Reynolds numbers of 2.6×10^5 and 9.3×10^5 for $T_w/T_t = 0.4$ will be presented. The model chamber pressures used for these tests were approximately 210 and 300 psia for $N_{Re,\infty} = 2.6 \times 10^5$ and 400 psia for $N_{Re,\infty} = 9.3 \times 10^5$; hence the injection flow rates correspond to those shown in figure 15.

Results for $N_{Re,\infty} = 2.6 \times 10^5$.- The predictions of heating rates and the experimental data for $N_{Re,\infty} = 2.6 \times 10^5$ are shown in figures 16(a) and 16(b) for $p_c = 210$ and 300 psia, respectively. The hatched bands in these figures are bounded by the upper and lower limits of the predicted heat-transfer rates for the minimum and maximum limits in $\dot{m}$ obtained from the boundaries of the shaded bands of figures 15(a) and 15(b). Note that the lower limit of $\dot{m}$ gives the upper limit of heating rate and vice versa. The experimental data are shown as the vertical bars. The length of these bars represents the variation of heating rates measured within the same span interval $8.85 \leq z/d \leq 12.85$. Since measurements of recovery temperature with blowing were not available, all experimental data and theoretical results with blowing have been normalized with the local theoretical heating rates for no blowing. These reference values of
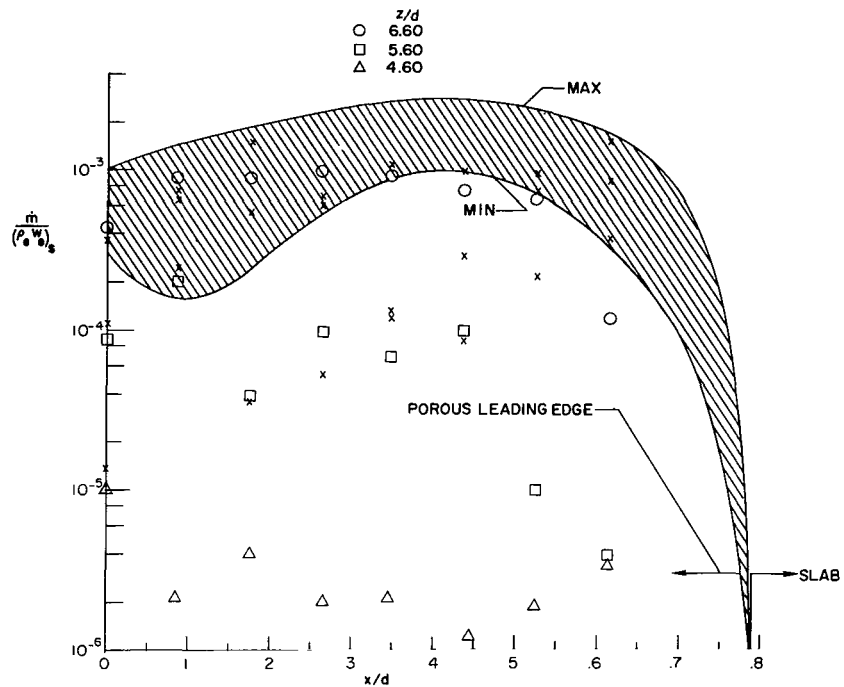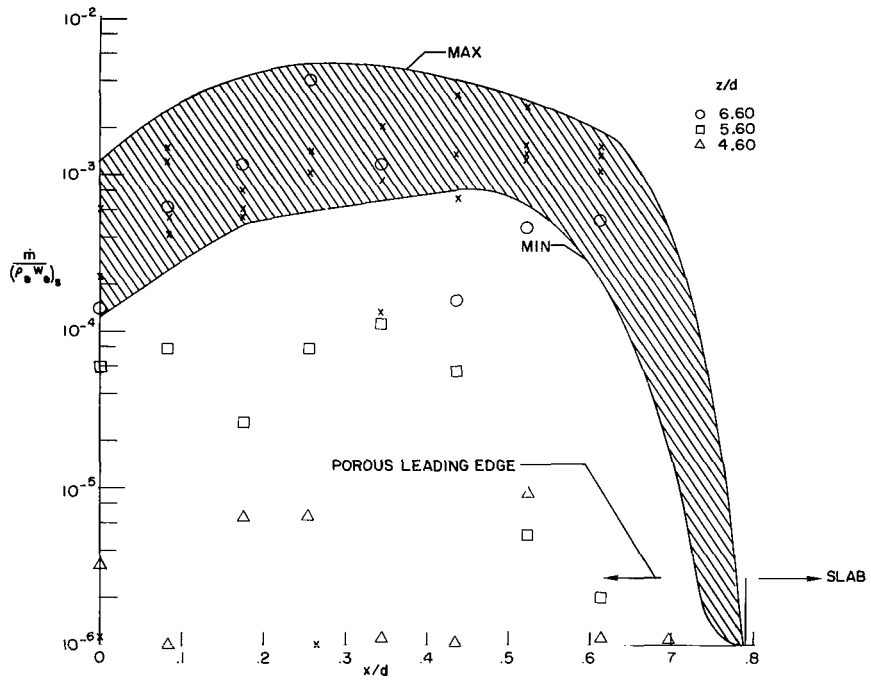
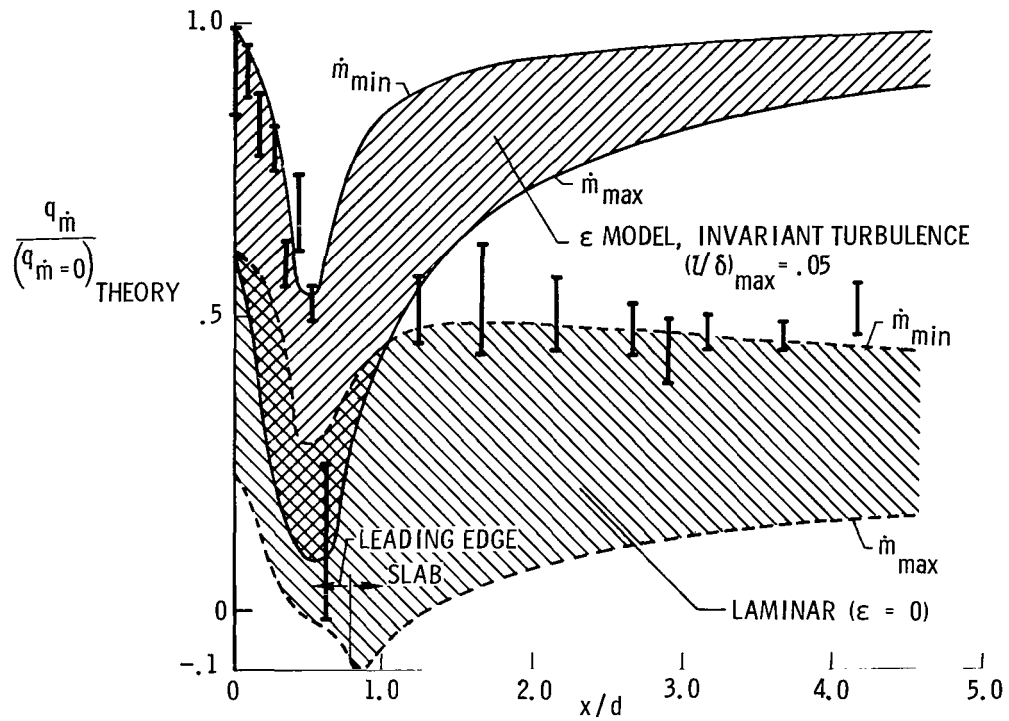(a) $p_c = 212$ psia; $N_{Re,\infty} = 2.6 \times 10^5$.
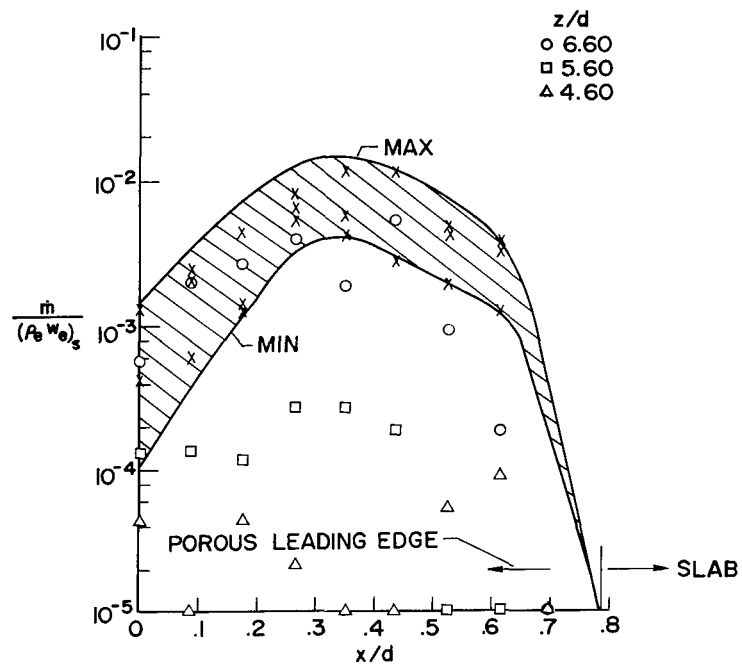
(b) $p_c \approx 300$ psia; $N_{Re,\infty} = 2.6 \times 10^5$.

Figure 15.- Experimental chordwise variation of mass flow through porous leading edge. Hatched band is for $7.85 \leqq z/d \leqq 12.85$. The x symbols indicate values measured at locations of thermocouple junctions within the same z/d interval.
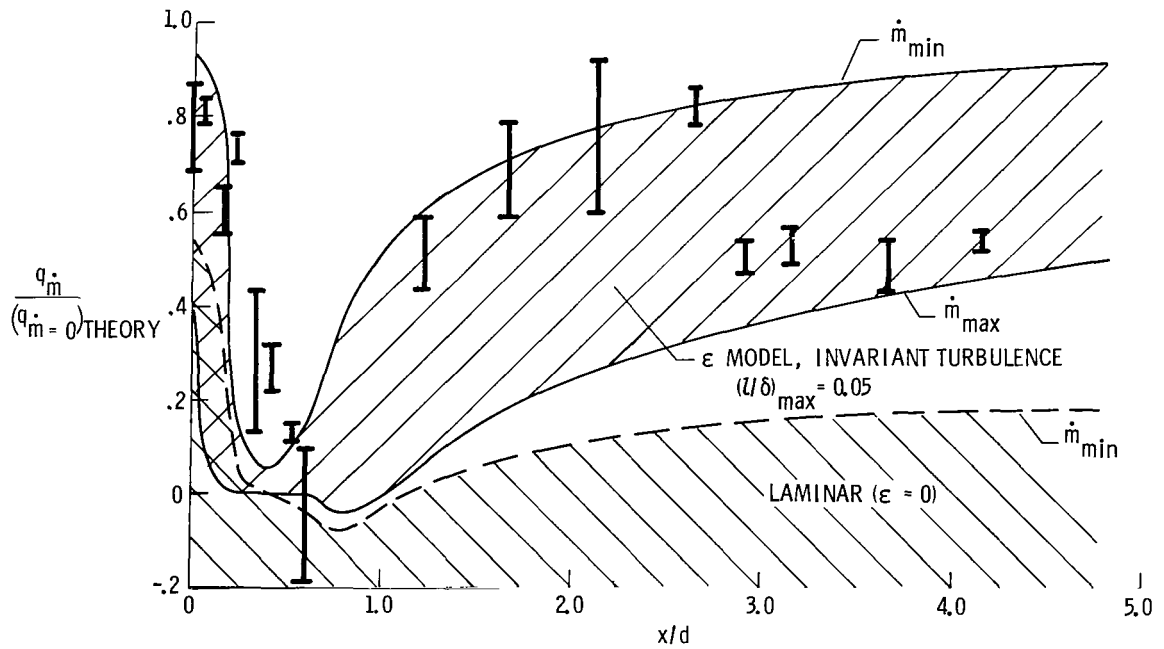
(c) p_c = 405 psia; $N_{Re,\infty}$ = 9.3 × 10^5.

Figure 15.- Concluded.

(a) $p_c \approx 210$ psia.

(b) $p_c \approx 300$ psia.

Figure 16.- Effect of blowing on chordwise heat transfer. Bars indicate experimental data spread. $N_{Re,\infty} = 2.6 \times 10^5$; $8.85 \leqq z/d \leqq 12.85$.

heating rates for no blowing were computed for the same local values of T_w that occurred in the test data or were used in the theory with blowing. All reference values of heating rate in this and subsequent figures were computed with the invariant-turbulence eddy-viscosity model and $(l/\delta)_{max} = 0.05$.

Comparison of the experimental and theoretical heat-transfer results in figure 16(a) indicates that the boundary layer on the leading edge is turbulent and that the data agree with predictions for minimum injection rates rather than those for maximum injection rates. Just upstream of the slab interface, the experimental heating rates decrease and are within the predicted laminar limits. The data on the slab agree with laminar predictions for the minimum injection rates. These trends suggest the possibility of laminarization of the initially turbulent boundary layer on the leading edge, as was indicated by the results for no blowing (figs. 9(a), 10(a), and 13(a)). The negative heating rates predicted by the theory for laminar flow with maximum blowing rates in the vicinity of $x/d \approx 0.8$ are caused by the large expansion of the flow around the leading edge. This large expansion reduces the static temperature of the injected film of air near the surface below its temperature farther upstream (which would be almost the wall temperature). Hence, when this surface film of air is convected downstream, its temperature is below the local surface temperature, and heat is then conducted from the model to the flow.

Comparison in figure 16(b) of the experimental and theoretical results for larger blowing rates (corresponding to $p_c \approx 300$ psia shown in fig. 15(b)) again indicates that the boundary layer on the leading edge was turbulent and the experimental data tend to agree with predictions for minimum injection rates. No solution could be obtained for the maximum injection rate with laminar flow apparently because "blowoff" or boundary-layer separation would have occurred. In contrast with the data of figure 16(a), however, the data of figure 16(b) show that turbulent flow persists farther downstream on the slab to $x/d \approx 2.5$. This downstream movement of turbulent flow may be caused by the destabilizing influence of the increased blowing rates (corresponding to the increase in p_c from 210 to 300 psia).

The rather abrupt drop in heating from $x/d = 2.65$ to $x/d = 2.90$ may be caused by the smaller upstream blowing rates imposed on the flow over the thermocouples located in the range of $x/d \geqq 2.90$. To clarify this statement, the thermocouple locations on the slab are identified in figure 17 according to whether $x/d \geqq 2.90$ or $x/d \leqq 2.65$. The inviscid and surface viscid (both laminar and turbulent) streamlines which leave the porous leading edge at $z/d = 7.85$ are also shown in the figure. Comparison of these streamline patterns with the two groups of thermocouple locations shows that the flow over most of the thermocouple locations for $x/d \geqq 2.90$ originates farther
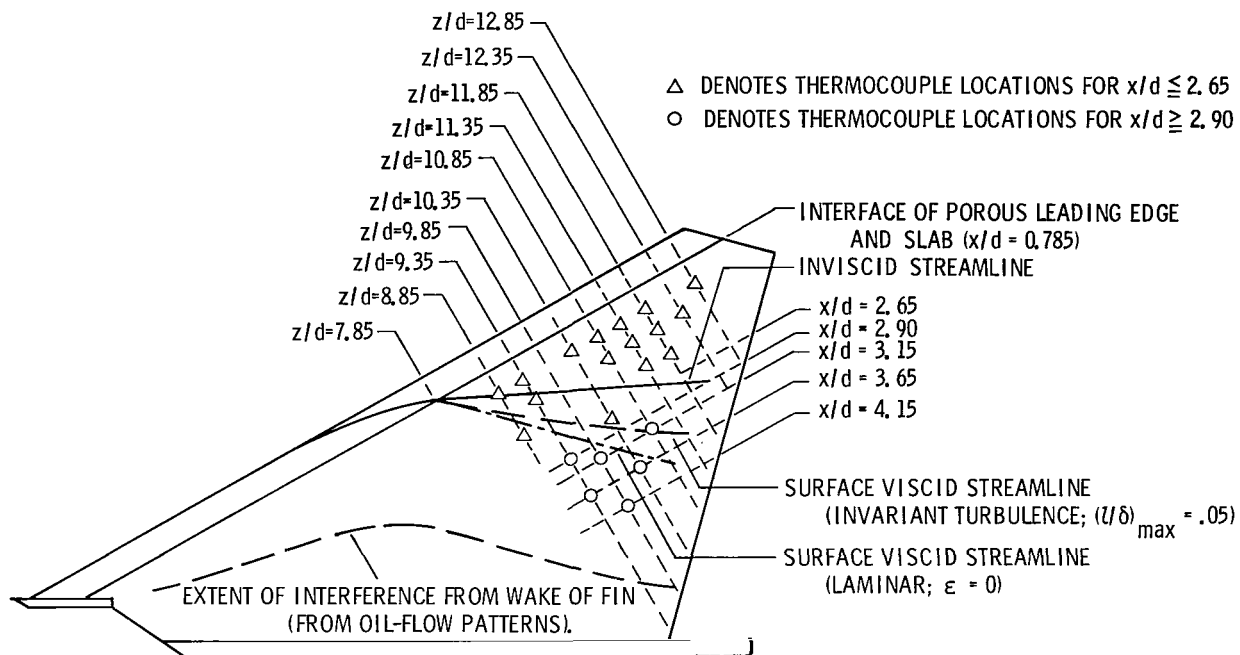
Figure 17.- Thermocouple positions on slab of porous-leading-edge model grouped according to whether $x/d \geqq 2.90$ or $x/d \leqq 2.65$ with inviscid and viscid streamlines exiting porous leading edge at $z/d = 7.85$.

inboard on the leading edge than the flow over the thermocouples for $x/d \leq 2.65$. The inboard flow is subjected to smaller blowing rates than the outboard flow, as indicated by the data in figure 15(b) for $z/d < 7.85$. The smaller blowing rates for the inboard flow may then account for the trend of reduced heating for $x/d \geqq 2.90$.

The agreement of data on the slab with predicted heat transfer for minimum leading-edge blowing is attributed to the reduced levels of injection rates as z/d is reduced. (Some of these smaller injection rates for $z/d < 7.85$ are shown in figs. 15(a) and 15(b).) The origin of a given streamline on the porous leading edge is far inboard of the z/d position at which it passes onto the slab. (See fig. 17.) The average blowing rate over the path of a streamline on the porous leading edge is generally smaller than that measured at the outboard z/d stations because of the spanwise variation in permeability.

The reduction in blowing rates for $z/d \leq 7.85$ may also affect measured heating rates on the leading edge for $z/d > 7.85$. That is, the local heating rates would tend to be larger because of the upstream history of small blowing rates along streamlines. Another factor which must be considered is the possible effect of some local blockage of the coolant flow in the vicinity of the thermocouple junction. That is, the measured mass flow rates at these thermocouple locations tend to be somewhat smaller than most of the other measured flow rates within the span interval $7.85 \leq x/d \leq 12.85$ as indicated in

figure 15(a), where the data points obtained at the junction locations are shown as x symbols. Data for the larger blowing rates, to be considered subsequently, indicate that local blockage of the coolant flow is not a major factor in the measured heating rates.

As mentioned previously, the heat-transfer results shown in figure 16(a) for the smallest blowing-rate distribution (fig. 15(a)) indicate the same apparent laminarization trends noted for the same value of $N_{Re,\infty}$ in the data for no blowing (figs. 9(a), 10(a), and 13(a)). Keeping the Reynolds number constant and increasing the blowing rate to that shown in figure 15(b) apparently caused turbulent flow to persist farther downstream (fig. 16(b)). The reduced heating for $x/d > 2.90$ for this case may be attributed to the history of reduced blowing rates for these streamlines. These results indicate that a blowing-rate "threshold" exists. Below this threshold, leading-edge blowing has no significant effect on laminarization. Blowing rates above this threshold may affect the response of a turbulent boundary layer to stabilizing influences and delay the development of laminarization trends.

Results for $N_{Re,\infty} = 9.3 \times 10^5$.- The chamber pressure for the tests at $N_{Re,\infty} = 9.3 \times 10^5$ was held at $p_c \approx 400$ psia. The predictions and experimental data are shown in figure 18, where the same format for data and theory as that of figure 16 is
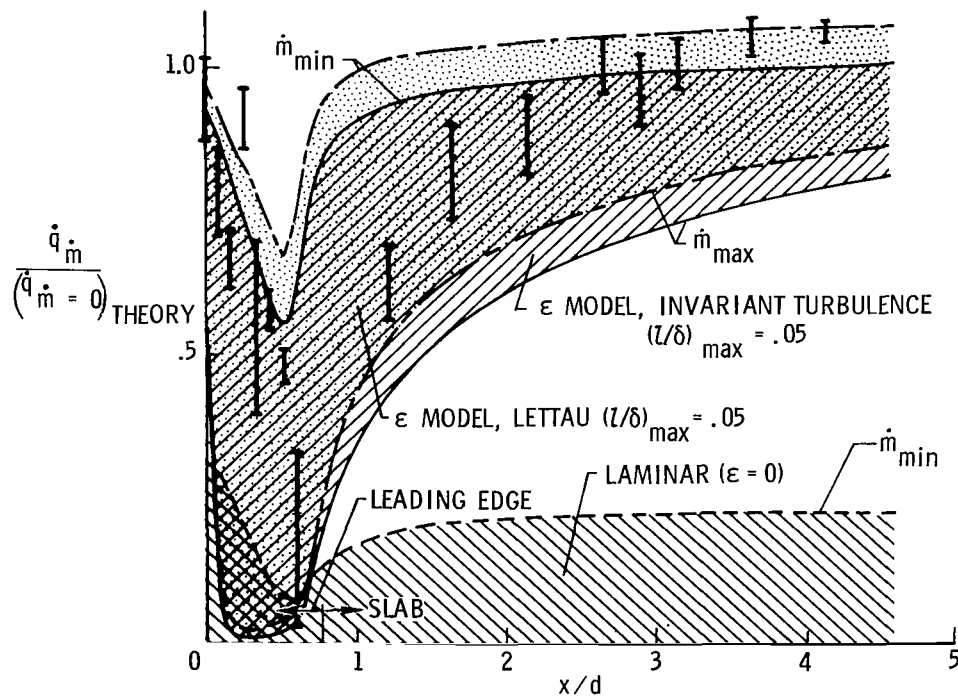

Figure 18.- Effect of blowing on chordwise heat-transfer distribution. Bars indicate experimental data spread. $N_{Re,\infty} = 9.3 \times 10^5$; $p_c \approx 400$ psia; $8.85 \leqq z/d \leqq 12.85$.

used. Again, no solution could be obtained for the maximum injection rate with laminar flow apparently because blowoff or boundary-layer separation would have occurred. The predicted ratios of heating rates for the minimum injection flow with the Lettau eddy-viscosity model exceed unity over most of the slab because the reference $\dot{q}_{m=0}$ is for the invariant-turbulence model.

Comparison of data and predictions shown in figure 18 again indicates that the flow was turbulent on the leading edge with measured heating levels near the predictions for minimum blowing. Here the theoretical turbulent prediction with the invariant-turbulence assumption and $(l/\delta)_{max} = 0.05$ is in best agreement with the data. The large decrease in the measured heating just upstream of the slab is probably again caused by laminarization. Following this minimum, the heating on the slab increases rapidly toward the predicted turbulent levels for minimum blowing. Both eddy-viscosity models give heating predictions within the spread of the data for $x/d \gtrsim 2.50$. The tendency of the data on the slab to agree with predictions for minimum blowing rates at the leading edge is again attributed to the reduction in blowing with decreasing z/d. (See fig. 15(c).) These results are therefore consistent in every respect with the no-blowing results at the same Reynolds number. (Compare figs. 9(b), 10(b), 12(b), and 13(b).) Apparently, this blowing level has not significantly affected the laminarization effects or transition location. The tendency of the data on the leading edge to agree with predictions for minimum blowing rates is also consistent with the blowing data at the lower Reynolds number (fig. 16) but is apparently caused mainly by the spanwise variations in blowing (note data beneath shaded bands in fig. 15) rather than by the partial blockage of the injected air at the thermocouples as suggested by the lower blowing rate distribution (x-symbols in fig. 15(a)), since the flow rates at locations of thermocouple junctions (x-symbols in figs. 15(b) and 15(c)) indicate practically no partial blockage for these higher blowing distributions.

Effects of blowing in the stagnation region for turbulent flow.- Solutions with the invariant-turbulence eddy-viscosity model with $(l/\delta)_{max} = 0.05$ were obtained by the finite-difference procedure for several blowing rates in addition to those shown in figure 15. The heat-transfer predictions in the vicinity of the stagnation line from these solutions are shown in figure 19. The ratios of $N_{St}/N_{St,\dot{m}=0}$ are plotted against the blowing parameter B/N_{St}, for which, as in reference 35, the recovery factor with blowing for both data and theory was taken as 0.9 of the recovery factor for no blowing.

The dashed line is a correlation of the computed values to within 1 percent for both test Reynolds numbers used in the computations. The experimental data are in reasonable agreement with the theoretical prediction over the range of blowing rates available. The blowing rates used for the data points were taken as the measured values at the corresponding thermocouple locations.
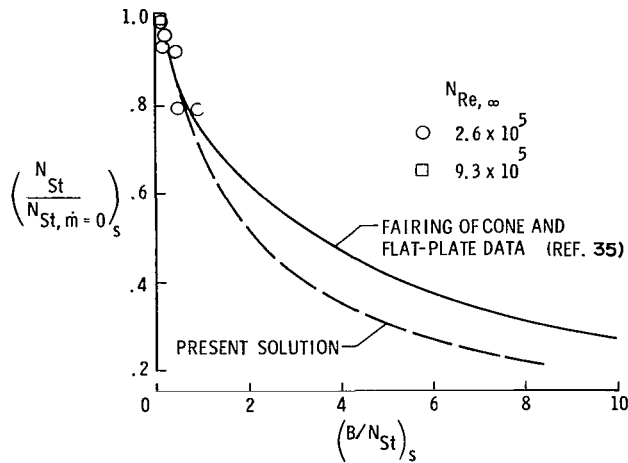
44

Figure 19.- Effect of blowing in the stagnation region
for turbulent flow. $x/d \approx 0.1$.

Also shown for comparison in figure 19 is a correlation in terms of the same parameters for flat-plate and cone data. These data are for turbulent boundary layers and the correlation is obtained from reference 35. The blowing rates for the present data are too small to provide a reliable assessment of the prediction. However, comparison of the correlation lines indicates that blowing near the stagnation line of swept cylinders reduces the heating more than a comparable blowing rate on flat plates.

Cross-Flow Predictions

As mentioned in the Introduction, the use of an inviscid-streamline coordinate system and the assumption of small cross flow simplify the boundary-layer equations. That is, the momentum equation in the streamwise direction and the energy equation become independent of the cross flow. If the inviscid streamlines are known, the problem is therefore reduced to the solution of an equivalent two-dimensional flow.

In order for the assumption of small cross flow to be generally valid, the square of the ratio of the cross-flow velocity to the streamwise velocity must be small. The maximum value of this ratio occurs at the limit as $y \to 0$ (see refs. 5 and 6, for example). The small-cross-flow criterion is then

$$\left(\frac{\tau_n}{\tau_p}\right)_w^2 \ll 1.0 \tag{31}$$

In the present notation this shear-ratio parameter is

$$\frac{\tau_n}{\tau_p} = \tan\left(\theta_w - \theta_e\right) \tag{32}$$

45

where θ_e is the angle between the spanwise coordinate direction and the local inviscid streamline direction, and $\theta_w = \arc\tan\left(\dfrac{\tau_x}{\tau_z}\right)_w$.

The chordwise distributions of the small-cross-flow parameter $\left(\tau_n/\tau_p\right)_w^2$ from several of the same solutions used in previous figures are shown in figure 20. The maximum values in the curves occur near the interface of the leading edge and slab and range from 0.17 to 0.28 for turbulent flow with no blowing. These results are consistent with the location and magnitude of maximum values of the cross-flow parameter obtained by Bradley (ref. 5) for turbulent flow on a circular cylinder at higher Reynolds numbers. These peak values from reference 5 were approximately 0.12.

The distributions from the solutions for laminar flow with no blowing are essentially independent of Reynolds number and the maximum value is 0.44, which is in agreement with corresponding values obtained in reference 6. The results given in reference 6 are for laminar boundary layers on circular cylinders with the assumption of local similarity. Interpolation between the results of reference 6 gives a maximum value for the cross-flow parameter of about 0.4 for the present conditions.

The effect of blowing increases the values of the cross-flow parameter by as much as an order of magnitude when the maximum blowing rates are used. For these conditions, the assumption of small cross flow would not be applicable to the momentum
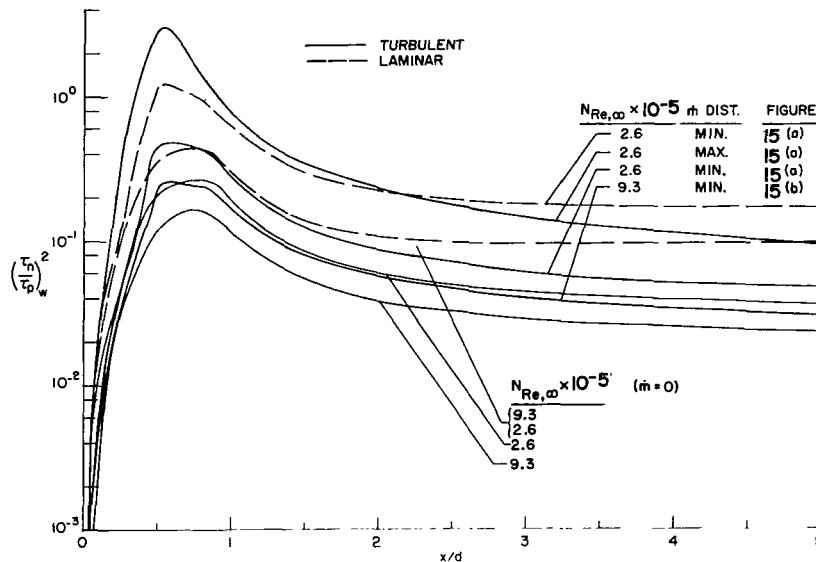

Figure 20.- Chordwise distribution of small-cross-flow parameter from theory. Invariant-turbulence model with $(l/\delta)_{max} = 0.05$ used for turbulent computations.

46

characteristics of the boundary layer such as velocity profiles, skin friction, and surface streamlines. However, the results of reference 6 indicated that heat-transfer predictions from the small cross-flow theory for laminar boundary layers were within 15 percent of the correct values when the cross-flow parameter was as large as 3.0.

CONCLUSIONS

A finite-difference method has been developed to solve the equations for compressible turbulent boundary layers on swept infinite cylinders. Predictions of surface heat transfer by this method were compared with experimental data on a blunt slab configuration with and without leading-edge blowing. The leading edge was a hemicylinder which was swept 60° with respect to the free-stream flow direction.

Predictions from the finite-difference method for solving the boundary-layer equations were also compared with experimental values of surface streamlines, Mach number profiles, boundary-layer thickness, and heat transfer on a similar configuration but without blowing. The tests were conducted at a free-stream Mach number of 8 and over a range of free-stream Reynolds numbers based on leading-edge diameter $N_{Re,\infty}$ of 0.92×10^5 to 9.3×10^5.

Two eddy-viscosity models which utilized general mixing-length functions scaled to the boundary-layer thickness were used in the calculations. One was termed the "invariant turbulence" model and was a scalar function based on the assumption that eddy viscosity is independent of direction. The other model was based on Lettau's vorticity-transfer hypothesis (Journal of the Atmospheric Sciences, vol. 21, no. 4, July 1964) and was also independent of direction but contained the scalar sum of two velocity-gradient terms.

A numerical procedure for solving the two-dimensional heat conduction problem in a porous matrix with one-dimensional fluid flow was also developed. This procedure was used to reduce the temperature-time history of the thermocouples near the surface of the porous leading edge to surface heat-transfer rates.

The main conclusions from the investigation are as follows:

1. The finite-difference method gave reasonable predictions for heat transfer, surface streamlines, Mach number profiles, and boundary-layer thickness on the test configuration without blowing for both laminar and turbulent flow. Reasonable predictions for heat transfer on both the leading edge and slab were also obtained with nonuniform, discontinuous blowing at the leading edge.

2. Comparisons of experimental and theoretical heat-transfer results indicate that the boundary layer on the leading edge of the 60° swept slab is turbulent for both $N_{Re,\infty} = 2.6 \times 10^5$ and 9.3×10^5.

3. For no blowing, the turbulent boundary layer was apparently laminarized just aft of the leading edge. At $N_{Re,\infty} = 2.6 \times 10^5$, the boundary layer remained essentially laminar to the end of the slab (5 nose diameters along the chord from the leading edge). At $N_{Re,\infty} = 9.3 \times 10^5$ apparent transition back to turbulent flow occurred about 2 diameters from the leading edge. Predictions from both eddy-viscosity models for maximum values of the ratio of the mixing length to the boundary-layer thickness $(l/\delta)_{max}$ of 0.05 were then in reasonable agreement with the data. These results were based on comparisons of theoretical predictions with all measured quantities mentioned above.

4. For the smallest blowing rates used in this investigation, leading-edge blowing had no appreciable effect on either the apparent laminarization phenomena or transition. However, for $N_{Re,\infty} \doteq 2.6 \times 10^6$, when the blowing rates were increased by about 40 percent, turbulent flow apparently persisted to about 2 leading-edge diameters farther downstream than for the small blowing rates. These results indicate that blowing had little effect on apparent laminarization until some blowing rate threshold was exceeded.

5. Comparison of values for a laminarization criterion indicated that the turbulent boundary layer on the leading edge for these tests was much more susceptible to laminarization than a comparable conical nozzle flow. This increased susceptibility to laminarization is tentatively attributed to the low turbulence levels of the boundary layer on the leading edge as evidenced by the relatively small values of $(l/\delta)_{max}$ required to obtain agreement of theory with experiment.

6. Measured heat-transfer rates on the leading edge over a 4-inch span interval agreed with values predicted for the minimum injection rates measured on the leading edge over the same 4-inch interval. This agreement with predictions for minimum injection was attributed mainly to the smaller injection rates near the apex of the leading edge. The influence of the partial blockage of injection at the thermocouple locations on the leading edge was considered minor.

7. Downstream of the leading edge on the thin-skinned slab, the measured heating rates were also generally in agreement with predictions for the minimum injection rates on the leading edge. These results are attributed to the smaller injection rates near the apex of the leading edge due to the spanwise distribution of permeability.

8. Blowing on the leading edge increased the magnitude of the cross-flow velocities by as much as an order of magnitude. Therefore, the assumption of small cross flow, which was not used in the present method, would not be expected to provide reliable predictions for the momentum characteristics of boundary layers with large leading-edge blowing.

Langley Research Center,
    National Aeronautics and Space Administration,
        Hampton, Va., January 28, 1971.

APPENDIX A

A HEAT-BALANCE METHOD FOR THE INVERSE SOLUTION OF

TWO-DIMENSIONAL HEAT CONDUCTION IN A POROUS

MATRIX WITH ONE-DIMENSIONAL FLUID FLOW

A numerical procedure was developed to reduce the temperature-time histories of each thermocouple within the porous wall to heating rates. The method provides an approximate solution of the two-dimensional heat-conduction problem in a porous matrix with one-dimensional (or radial) fluid flow and with temperature-dependent thermal properties. The temperature of the fluid is assumed to be the same as that of the porous matrix.

To illustrate the procedure, consider the finite slab shown divided into six blocks in figure 21. The upper and lower surfaces of the slab are insulated. The initial temperature and time-dependent one-dimensional blowing rates for each block are known. At time $t = t_0$, the front face of the slab (the left side in the figure) is exposed to an unknown heating rate which may vary with time and block location. The temperature change with time at

BLOCK CONFIGURATION WITH HEAT AND MASS FLUX $\left(\frac{\partial}{\partial z} = 0 \right)$
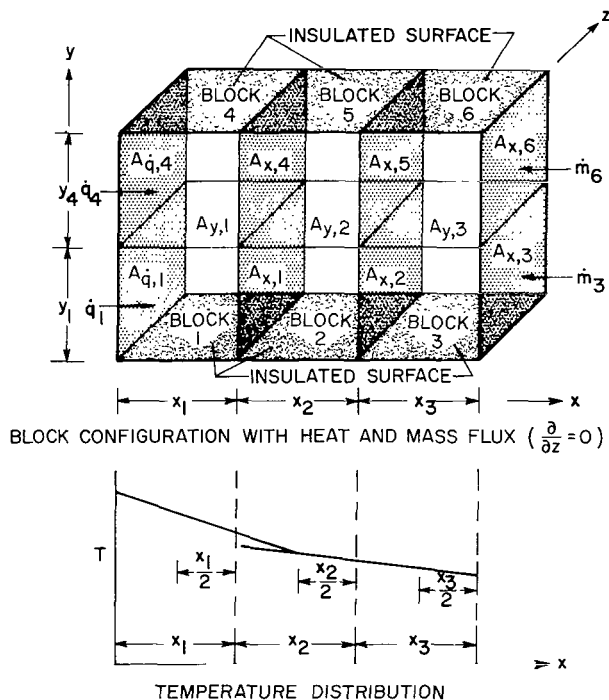
TEMPERATURE DISTRIBUTION

Figure 21.- Sketch of six-block heat-conduction model to illustrate method and notation. Model is assumed two dimensional; that is, derivatives of all quantities in z-direction are zero.

the midpoint of both surface blocks is measured. In order to determine the temperature-time profiles of the remaining blocks, a heat balance is written for each. In the heat stored term each block is assumed to be at a uniform temperature throughout its volume. In the heat conduction and gas absorption terms, a linear temperature variation between centers of blocks is assumed. The heat balance for block 1 is as follows:

$$
\underset{\text{Con-vection}}{\dot{q}_1 A_{\dot{q},1}} - \underset{\text{Radiation}}{A_{\dot{q},1}\epsilon^*\sigma\left(T'_{A_{\dot{q},1}}\right)^4} - \underset{\text{Stored}}{\rho_1 c_1 V_1 \frac{(T_1 - T'_1)}{\Delta t}} - \underset{\text{Gas absorbed}}{2\dot{m}_3 A_{x,3} c_{p,1} \frac{x_1(T_1 - T_2)}{(x_1 + x_2)}} - \underset{\substack{\text{x conducted,}\\\text{material}}}{2\bar{k}_{1,2} A_{x,1} \frac{(T_1 - T_2)}{(x_1 + x_2)}}
$$

$$
\underset{\text{x conducted, gas}}{- 2(\bar{k}_g)_{1,2} A_{x,1} \frac{(T_1 - T_2)}{(x_1 + x_2)}} - \underset{\text{y conducted, material}}{2(\bar{k}_g)_{1,4} A_{y,1} \frac{(T_1 - T_4)}{(y_1 + y_4)}} - \underset{\text{y conducted, gas}}{2(\bar{k}_g)_{1,4} A_{y,1} \frac{(T_1 - T_4)}{(y_1 + y_4)}} = 0 \tag{33}
$$

where the primes denote a temperature evaluated at the previous time step and the subscripts 1 to 6 refer to block numbers. The subscript $\dot{q}$ indicates the surface exposed to heating rate $\dot{q}$. Since the calculation starts at $t = t_0$, all the primed quantities are known. A similar heat balance is written for all blocks and the resulting system of linear equations are

$$
\left.\begin{aligned}
a_1 T_1 + b_1 T_2 \quad\quad + d_1 T_4 \quad\quad\quad\quad &= -A_{\dot{q},1}\dot{q}_1 + g_1 \\
a_2 T_1 + b_2 T_2 + c_2 T_3 \quad\quad + e_2 T_5 \quad\quad &= g_2 \\
b_3 T_2 + c_3 T_3 \quad\quad\quad + f_3 T_6 &= g_3 \\
a_4 T_1 \quad\quad\quad\quad + d_5 T_4 + e_4 T_5 \quad\quad &= g_4 - A_{\dot{q},4}\dot{g}_4 \\
b_5 T_2 \quad\quad + d_5 T_4 + e_5 T_5 + f_5 T_6 &= g_5 \\
+ c_6 T_3 \quad\quad + e_6 T_5 + f_6 T_6 &= g_6
\end{aligned}\right\} \tag{34}
$$

The temperatures T_1 and T_4 are known; that is, they are obtained from the measured temperatures. Also, the temperature coefficients $a_i, b_i, \ldots, f_i$ and the constants g_i are calculated from the given inputs. The unknowns are then $\dot{q}_1$, $\dot{q}_4$, T_2, T_3, T_5, and T_6 which may be obtained from the solution of the following determinant system:

Unknowns

$\dot{q}_1$	T_2	T_3	$\dot{q}_4$	T_5	T_6	Constants for any n time step	
		Determinant elements					
$A_{\dot{q},1}$	b_1	0	0	0	0	$-a_1 T_1 - d_1 T_4 + g_1$	
0	b_2	c_2	0	e_2	0	$-a_2 T_1 + g_2$	(35)
0	b_3	c_3	0	0	f_3	$+g_3$	
0	0	0	$A_{\dot{q},4}$	e_4	0	$-a_4 T_1 - d_4 T_4 + g_4$	
0	b_5	0	0	e_5	0	$-d_5 T_4 + g_5$	
0	0	c_6	0	e_6	f_6	$+g_6$	

This system is solved successively at each n time step where $t = t_0 + n\Delta t$. The values of the specific heats and thermal conductivities are "updated" at the new temperatures obtained after each time step. The coefficients and constants of the determinant can then be updated, and the heating rates and temperature distributions obtained for the next time step. This procedure is repeated until a specified time interval $t_f = t_0 + j\Delta t$ is reached. The surface heating rates for each block are thereby computed over this specified time interval with the time-dependent inputs T_1, T_4, $\dot{m}_6$, and $\dot{m}_3$ and the temperature-dependent material properties.

Two different block configurations were used for five spanwise stations on the porous leading edge, as shown in figure 22. These block configurations were set up so that experimental thermocouple readings could be used as direct inputs to the computer program without smoothing techniques applied to the data. Hence, the chordwise thermocouple distributions at the spanwise stations as indicated in the figure determined the block configurations because the temperature-time history for one block in each column of blocks is required as an input to the program. In the 56-block configuration, the symmetry of the thermocouple locations about the $x/d = 0$ station allowed the use of the "surface" thermocouple readings at both the location of the thermocouple and its "mirror" image. This increase in the number of columns from four to seven was made in order to reduce the chordwise length of the blocks and still provide thermocouple data in the chordwise center of each column of blocks. Superposition of the thermocouple locations in this manner is strictly valid only if the chordwise distribution of permeability α is perfectly symmetrical. Deviations in α from symmetry can be obtained from figure 14 where the
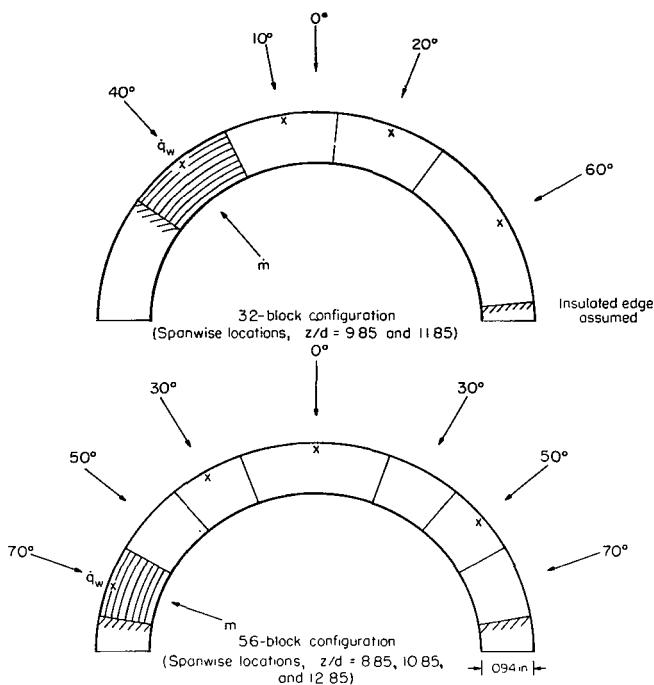
Figure 22.- Block configurations used to reduce data from porous leading
   edge. Thermocouple locations are given in table II and designated as
   x   in sketch.

data for the x locations of 10°, 30°, 40°, and 70° are shown as flagged symbols. These
deviations are small for most of the data and hence were neglected in the 56-block
configuration.

The chordwise conduction errors are small, in spite of the relatively large block
dimensions in the chordwise plane, because of the nearly isothermal conditions during
the short test period. The boundary condition of the insulated edge (fig. 22) will cause a
slight reduction in the heating rates calculated for the two edge blocks compared with that
which occurred in the tests since no such restriction applied to the experimental model.

The surface block of each column was made 0.004 inch thick in accordance with the
approximate depth of the thermocouple junction. The remaining thickness of approxi-
mately 0.090 inch was divided into seven blocks of equal thickness. The time step used
herein for all solutions was 0.05 second. Comparisons of results from calculations for
one-dimensional heat-conduction problems with exact solutions from Carslaw and Jaeger
(ref. 36) indicated that for the block thicknesses and time steps of the present computa-
tions, errors would have been negligible had only five equal-thickness blocks been used.
To assess further the reliability of the heat-balance method, tests were conducted on the
porous-leading-edge model with no mass injection at the same tunnel conditions for which
the phase-change heat-transfer technique was used on the plastic models. The validity

53

of the inverse heat-balance method was confirmed by comparisons of the resultant heat-transfer distributions. Description and verification of a one-dimensional inverse heat-balance solution without fluid flow is given in reference 37.

APPENDIX B

TECHNIQUE FOR MEASURING BLOWING-RATE DISTRIBUTION

ON POROUS LEADING EDGE

The local mass injection rates on the porous leading edge were measured at several spanwise stations and chordwise distances over a range of internal pressures from 150 to 400 psig. These measurements were made with a plastic tip probe (0.096 inch inside diameter) which was pressed against the porous surface as shown in figure 23. The probe
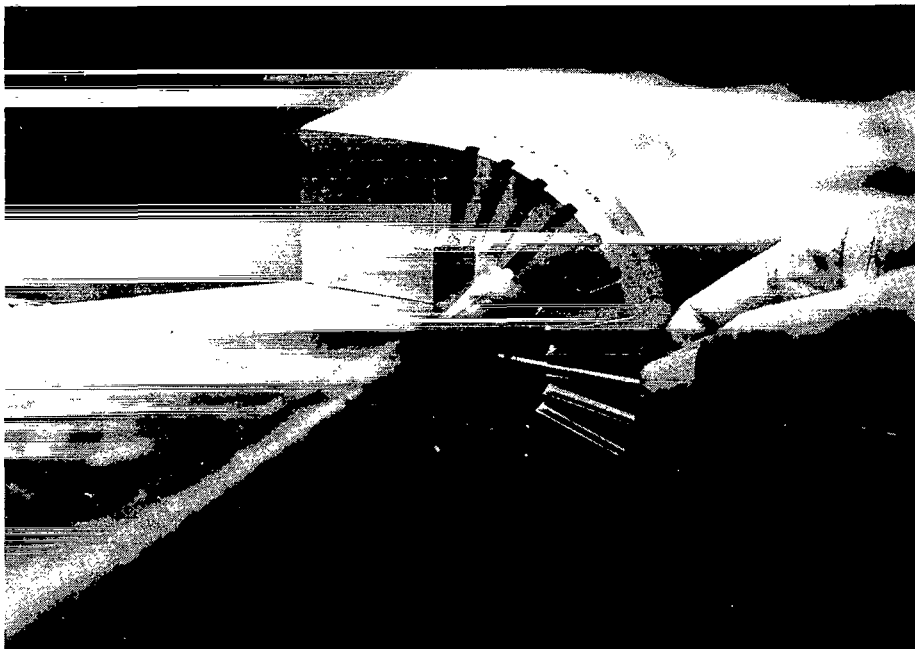
L-69-7057

Figure 23.- Plastic tip probe and alinement jig for measuring injection rates.

was connected with a butyl phthalate manometer and a pressure-sealed container of known volume. The total mass flow rate through the porous leading edge was set at the desired level by adjusting the internal pressure. This flow rate was measured with a floating ball-type flowmeter. The plastic tip probe was held in contact with the model for a measured period of time. At the end of this period ($\geq$ 30 sec) the system was sealed just downstream of the plastic tip probe. After equilibrium was established, the change in pressure and volume (the change in volume due to the change in level of the manometer fluid) of the isothermal system was recorded. The local mass flow rate through the contact area of 0.096-inch diameter could then be calculated. The pressure rise in the

sealed volume was limited to less than 0.7 percent of the pressure inside the model. Therefore, the mass-flow distribution through the porous material was not altered by the measurement technique. The validity of this statement is evident from the relation for the mass flow rate through a uniformly porous material. This relation is given in reference 38 (eq. (7), p. 78) and, in the notation herein, is

$$\dot{m} \equiv \rho_w v_w = \frac{\alpha}{2R(\mu T)_w} \frac{p_c^2 - p_w^2}{\Delta Y} \tag{36}$$

Measurements were made at chordwise intervals of 10° around the leading edge and at spanwise intervals of 1 inch or less along the porous leading edge in the region $7.85 \leq z/d \leq 11.85$.

REFERENCES

1. Braun, Willis H.: Turbulent Boundary Layer on a Yawed Cone in a Supersonic Stream. NASA TR R-7, 1959. (Supersedes NACA TN 4208.)

2. Nagel, A. L.; Fitzsimmons, H. D.; and Doyle, L. B.: Analysis of Hypersonic Pressure and Heat Transfer Tests on Delta Wings With Laminar and Turbulent Boundary Layers. NASA CR-535, 1966.

3. Beckwith, Ivan E.; and Gallagher, James J.: Local Heat Transfer and Recovery Temperatures on a Yawed Cylinder at a Mach Number of 4.15 and High Reynolds Numbers. NASA TR R-104, 1961. (Supersedes NASA MEMO 2-27-59L.)

4. Vaglio-Laurin, Roberto: Turbulent Heat Transfer on Blunt-Nosed Bodies in Two-Dimensional and General Three-Dimensional Hypersonic Flow. J. Aero/Space Sci., vol. 27, no. 1, Jan. 1960, pp. 27-36.

5. Bradley, Richard G.: Approximate Solutions for Compressible Turbulent Boundary Layers in Three-Dimensional Flow. AIAA J., vol. 6, no. 5, May 1968, pp. 859-864.

6. Beckwith, Ivan E.: Similarity Solutions for Small Cross Flows in Laminar Compressible Boundary Layers. NASA TR R-107, 1961.

7. Nash, J. F.: The Calculation of Three-Dimensional Turbulent Boundary Layers in Incompressible Flow. J. Fluid Mech., vol. 37, pt. 4, July 1969, pp. 625-642.

8. Bushnell, Dennis M.; and Beckwith, Ivan E.: Calculation of Nonequilibrium Hypersonic Turbulent Boundary Layers and Comparisons With Experimental Data. AIAA J., vol. 8, no. 8, Aug. 1970, pp. 1462-1469.

9. Hunt, James L.; Bushnell, Dennis M.; and Beckwith, Ivan E.: Finite-Difference Analysis of the Compressible Turbulent Boundary Layer on a Blunt Swept Slab With Leading-Edge Blowing. Analytic Methods in Aircraft Aerodynamics, NASA SP-228, 1970, pp. 417-470.

10. Lettau, H.: A New Vorticity-Transfer Hypothesis of Turbulence Theory. J. Atmos. Sci., vol. 21, no. 4, July 1964, pp. 453-456.

11. Reshotko, Eli; and Beckwith, Ivan E.: Compressible Laminar Boundary Layer Over a Yawed Infinite Cylinder With Heat Transfer and Arbitrary Prandtl Number. NACA TN 3986, 1957.

12. Schlichting, Hermann (J. Kestin, transl.): Boundary-Layer Theory. Sixth ed., McGraw-Hill Book Co., 1968.

13. Prandtl, L.: Report on Investigation of Developed Turbulence. NACA TM 1231, 1949.

14. Beckwith, Ivan E.: Recent Advances in Research on Compressible Turbulent Boundary Layers. Analytic Methods in Aircraft Aerodynamics, NASA SP-228, 1970, pp. 355-416.

15. Jones, Robert T.: Effects of Sweep-Back on Boundary Layer and Separation. NACA Rep. 884, 1947. (Supersedes NACA TN 1402.)

16. Young, A. D.; and Booth, T. B.: The Profile Drag of Yawed Wings of Infinite Span. Aero. Quart., vol. III, pt. III, Nov. 1951, pp. 211-229.

17. Ashkenas, Harry; and Riddell, Frederick R.: Investigation of the Turbulent Boundary Layer on a Yawed Flat Plate. NACA TN 3383, 1955.

18. Turcotte, Donald Lawson: On Incompressible Turbulent Boundary Layer Theory Applied to Infinite Yawed Bodies. Graduate School Aero. Eng., Cornell Univ. (Contract AF 33 (038)-21406), Sept. 1955.

19. Prandtl, L. (Suppl. by K. Wieghardt): On a New Representation of Fully Developed Turbulence. Publ. No. 13, Jet Propulsion Lab., California Inst. Technol., Aug. 1952. (Translation of "Über ein neues Formelsystem für die ausgebildete Turbulenz." Nachrichten der Akademie der Wissenschaften, Göttingen, Mathematisch-Physikalische Klasse, 1945.)

20. Glushko, G. S.: Turbulent Boundary Layer on a Flat Plate in an Incompressible Fluid. Bull. Acad. Sci. USSR, Mech. Ser. no. 4, 1965, pp. 13-23.

21. Bradshaw, P.: Calculation of Boundary-Layer Development Using the Turbulent Energy Equation. VII: Three-Dimensional Flow. NPL Aero Rep. 1286, Brit. A.R.C., Jan. 30, 1969.

22. Lettau, Heinz H.: New Hypothesis for the Relationship Between Eddy and Mean States. Phys. Fluids Suppl., vol. 10, pt. II, no. 9, Sept. 1967, pp. S79-S83.

23. Rotta, J. C.: Heat Transfer and Temperature Distribution in Turbulent Boundary Layers at Supersonic and Hypersonic Flow. AGARDograph 97, Pt. 1, May 1965, pp. 35-63.

24. Johnson, Donald S.: Turbulent Heat Transfer in a Boundary Layer With Discontinuous Wall Temperature. Publ. No. 55 (OSR Tech. Note 55-289), Dep. Aeronaut., The Johns Hopkins Univ., Aug. 1955.

25. Beckwith, Ivan E.; and Bushnell, Dennis M. (With appendix C by Carolyn C. Thomas): Detailed Description and Results of a Method for Computing Mean and Fluctuating Quantities in Turbulent Boundary Layers. NASA TN D-4815, 1968.

26. Stainback. P. Calvin: Heat-Transfer Measurements at a Mach Number of 8 in the Vicinity of a 90° Interior Corner Alined With the Free-Stream Velocity.   NASA TN D-2417, 1964.

27. Jones, Robert A.; and Hunt, James L.:   Use of Fusible Temperature Indicators for Obtaining Quantitative Aerodynamic Heat-Transfer Data.   NASA TR R-230, 1966.

28. Bushnell, Dennis M.:   Effects of Shock Impingement and Other Factors on Leading-Edge Heat Transfer.   NASA TN D-4543, 1968.

29. Bushnell, Dennis M.:   Interference Heating on a Swept Cylinder in Region of Intersection With a Wedge at Mach Number 8.   NASA TN D-3094, 1965.

30. Bradshaw, P.:   The Analogy Between Streamline Curvature and Buoyancy in Turbulent Shear Flow.   J. Fluid Mech., vol. 36, pt. 1, Mar. 1969, pp. 177-191.

31. Boldman, Donald R.; Schmidt, James F.; and Gallagher, Anne K.:   Laminarization of a Turbulent Boundary Layer as Observed From Heat-Transfer and Boundary-Layer Measurements in Conical Nozzles.   NASA TN D-4788, 1968.

32. Back, L. H.; Cuffel, R. F.; and Massier, P. F.:   Laminarization of a Turbulent Boundary Layer in Nozzle Flow — Boundary Layer and Heat Transfer Measurements With Wall Cooling.   Pap. No. 69-HT-56, Amer. Soc. Mech. Eng., Aug. 1969.

33. Gregory, N.; Stuart, J. T.; and Walker, W. S.:   On the Stability of Three-Dimensional Boundary Layers With Application to the Flow Due to a Rotating Disk.   Phil. Trans. Roy. Soc. (London), ser. A, vol. 248, no. 943, July 14, 1955, pp. 155-199.

34. Bushnell, Dennis M.; and Huffman, Jarrett K.:   Investigation of Heat Transfer to Leading Edge of a 76° Swept Fin With and Without Chordwise Slots and Correlations of Swept-Leading-Edge Transition Data for Mach 2 to 8.   NASA TM X-1475, 1967.

35. Baronti, Paolo; Fox, Herbert; and Soll, David: A Survey of the Compressible Turbulent Boundary Layer With Mass Transfer.   Astronaut. Acta, vol. 13, no. 3, May-June 1967, pp. 239-249.

36. Carslaw, H. S.; and Jaeger, J. C.:   Conduction of Heat in Solids.   Second ed., Oxford Univ. Press, Inc., 1959.

37. Howard, Floyd G.:   Single-Thermocouple Method for Determining Heat Flux to a Thermally Thick Wall.   NASA TN D-4737, 1968.

38. Muskat, M.:   The Flow of Homogeneous Fluids Through Porous Media.   First ed., second printing, J. W. Edwards, Inc., 1946.

TABLE I.- LOCATIONS OF PRESSURE ORIFICES USED

Chordwise location x/d at spanwise location z/d of —		
9.18	11.18	13.18
-0.524	-----	-0.524
-----	-0.439	-----
-.175	-----	-.175
-----	0	-----
.087	-----	.087
-----	.262	-----
.349	-----	.349
-----	.611	-----
.698	-----	.698
.911	.911	.911
1.411	1.411	1.411
2.161	2.161	2.161
3.161	3.161	3.161
-----	4.161	4.161
-----	5.161	5.161

TABLE II.- LOCATIONS OF THERMOCOUPLES ON
POROUS-LEADING-EDGE MODEL

Chordwise location x/d at spanwise location z/d of —								
8.85	9.35	9.85	10.35	10.85	11.35	11.85	12.35	12.85
-0.611	----	-----	----	-0.611	----	-----	----	-0.611
-----	----	-0.349	----	-----	----	-0.349	----	-----
-.262	----	-----	----	-.262	----	-----	----	-.262
-----	----	-.087	----	-----	----	-.087	----	-----
0	----	-----	----	0	----	-----	----	0
-----	----	.175	----	-----	----	.175	----	-----
.439	----	-----	----	.439	----	-----	----	.439
-----	----	.524	----	-----	----	.524	----	-----
1.223	1.223	-----	1.223	1.223	1.223	1.223	----	1.223
-----	1.650	-----	----	1.650	1.650	1.650	1.650	-----
2.150	----	-----	----	-----	2.150	2.150	----	-----
-----	----	-----	2.650	-----	----	-----	----	-----
-----	2.900	-----	----	-----	----	-----	----	-----
-----	----	3.150	----	3.150	----	-----	----	-----
-----	3.650	-----	3.650	-----	----	-----	----	-----
-----	----	4.150	----	-----	----	-----	----	-----

"*The aeronautical and space activities of the United States shall be conducted so as to contribute . . . to the expansion of human knowledge of phenomena in the atmosphere and space. The Administration shall provide for the widest practicable and appropriate dissemination of information concerning its activities and the results thereof.*"

— NATIONAL AERONAUTICS AND SPACE ACT OF 1958

NASA SCIENTIFIC AND TECHNICAL PUBLICATIONS

TECHNICAL REPORTS: Scientific and technical information considered important, complete, and a lasting contribution to existing knowledge.

TECHNICAL NOTES: Information less broad in scope but nevertheless of importance as a contribution to existing knowledge.

TECHNICAL MEMORANDUMS: Information receiving limited distribution because of preliminary data, security classification, or other reasons.

CONTRACTOR REPORTS: Scientific and technical information generated under a NASA contract or grant and considered an important contribution to existing knowledge.

TECHNICAL TRANSLATIONS: Information published in a foreign language considered to merit NASA distribution in English.

SPECIAL PUBLICATIONS: Information derived from or of value to NASA activities. Publications include conference proceedings, monographs, data compilations, handbooks, sourcebooks, and special bibliographies.

TECHNOLOGY UTILIZATION PUBLICATIONS: Information on technology used by NASA that may be of particular interest in commercial and other non-aerospace applications. Publications include Tech Briefs, Technology Utilization Reports and Technology Surveys.

Details on the availability of these publications may be obtained from:

SCIENTIFIC AND TECHNICAL INFORMATION OFFICE

NATIONAL AERONAUTICS AND SPACE ADMINISTRATION
Washington, D.C. 20546